ISSN: 2224-2007
E-ISSN: 2707-7365

MIJST

MIST International Journal of Science and Technology

A Peer Reviewed Online Open Access Journal

Volume 09
December 2021

Military Institute of Science and Technology (MIST)
https://mijst.mist.ac.bd/mijst
Previously known as:
MIST Journal of Science and Technology

MIJST

MIST International Journal of Science and Technology

EDITORIAL BOARD

CHIEF PATRON

Major General Md Wahid-Uz-Zaman, BSP, ndc, aowc, psc, te
Commandant
Military Institute of Science and Technology (MIST)
Dhaka, Bangladesh

PUBLICATION ADVISOR

Brigadier General Mohammad Pavel Akram, afwc, psc
Director, R&D Wing
Military Institute of Science and Technology (MIST)
Dhaka, Bangladesh

EDITOR-IN-CHIEF

Dr. Firoz Alam
Professor
School of Engineering, RMIT University
Melbourne, Australia

EXECUTIVE EDITOR

Dr. A.K.M. Nurul Amin
Professor, Industrial and Production Engineering
Military Institute of Science and Technology (MIST)
Dhaka, Bangladesh

ASSOCIATE EDITOR

Lt Col Md Altab Hossain, PhD, EME
Assoc. Professor, Nuclear Science and Engineering
Military Institute of Science and Technology (MIST)
Dhaka, Bangladesh

ASSOCIATE EDITOR

Lt Col Muhammad Nazrul Islam, PhD, Sigs
Assoc. Professor, Computer Science and Engineering
Military Institute of Science and Technology (MIST)
Dhaka, Bangladesh

EDITORIAL BOARD MEMBERS

Prof. G. M. Jahid Hasan
MIST, Bangladesh

Prof. Yuying Yan
Nottingham University, UK

Prof. Grzegorz Krolczyk
Opole University of Technology, Poland

Prof. Drazan Kozak
University of Slavonski Brod, Croatia

Assoc. Prof. Lt Col Khondaker Sakil Ahmed, PhD, PEng, CEng
MIST, Bangladesh

Prof. Sergej Hloch
Technical University of Košice, Slovakia

Prof. Mohamed H. M. Hassan
Alexandria University, Egypt

Prof. Xiaolin Wang
University of Tasmania, Australia

Prof. Md. Mahbubur Rahman
MIST, Bangladesh

Prof. Muhammad Mustafizur Rahman
Wichita State University, USA

Prof. Santanu Bandyopadhyay
Indian Institute of Technology (IIT) Bombay, India

Prof. Yan-Hui Feng
University of Science and Technology Beijing, China

Brig Gen A K M Nazrul Islam, PhD
MIST, Bangladesh

Prof. Stanislaw Legutko
Poznan University of Technology, Poland

Prof. Nakorn Tippayawong
Chiangmai University, Thailand

Prof. Katarina Monkova
Technical University of Košice, Slovakia & Tomas Bata University in Zlín, Czech Republic

Asst. Prof. Tariq Mahbub
MIST, Bangladesh

Prof. Elsadig Mahdi Ahmad Saad
Qatar University, Qatar

Prof. Himadri Chattopadhyay
Jadavpur University, India

Prof. Yingai Jin
Jilin University, China

Prof. M A Taher Ali
MIST, Bangladesh

Prof. Changheui Jang
Korea Advanced Institute of Science and Technology (KAIST), South Korea

Prof. Tanvir Farouk
University of South Carolina, USA

Prof. Abdul Hasib Chowdhury
BUET, Bangladesh

Assoc. Prof. Lt Col Osman Md Amin, PhD, Engrs
MIST, Bangladesh

Prof. Simon Watkins
RMIT University, Australia

Prof. Ataur Rahman
International Islamic University Malaysia, Malaysia

Prof. Somnath Chattopadhyaya
Indian Institute of Technology (IIT) Dhanbad, India

Assoc. Prof. Major Kazi Shamima Akter, PhD, Engrs
MIST, Bangladesh

Prof. Kaori Nagai
Nihon University, Japan

Prof. Alessandro Ruggiero
University of Salerno, Italy

Prof. Azam Ali
University of Otago, New Zealand

Assoc. Prof. Md. Sazzad Hossain
MIST, Bangladesh

Prof. Mohammed Quddus
Imperial College, UK

Prof. Anupam Basu
Indian Institute of Technology (IIT) Kharagpur, India

Prof. Muhammad H. Rashid
Florida Polytechnic University, USA

Prof. Md Enamul Hoque
MIST, Bangladesh

Prof. Naoya Umeda
Osaka University, Japan

Prof. Md Abdul Jabbar
University of Dhaka, Bangladesh

Prof. Soumyen Bandyopadhyay
Liverpool University, UK

Asst. Prof. Muammer Din Arif
MIST, Bangladesh

Prof. A.B.M. Harun-ur Rashid
BUET, Bangladesh

Prof. Shahjada Tarafder
BUET, Bangladesh

Prof. Mohammed Abdul Basith
BUET, Bangladesh

Prof. AKM Badrul Alam
MIST, Bangladesh

Prof. Stephen Butt
Memorial University of Newfoundland, Canada

Prof. Cheol-Gi Kim
Daegu Gyeongbuk Institute of Science & Technology, South Korea

Prof. Kawamura Yasumi
Yokohama National University, Japan

Assoc. Prof. Lt Col Brajalal Sinha, PhD, AEC
MIST, Bangladesh

Assoc. Prof. Lt Col Palash Kumar Sarker, PhD, Sigs
MIST, Bangladesh

Dr. Debasish Sarker
Bangladesh Army University of Science and Technology, Bangladesh

Prof. Nahrizul Adib Bin Kadri
University of Malaya, Malaysia

Lt Col Mirza Md Lutful Habib, SUP, psc, Engrs
General Staff Officer First Grade, R&D Wing, MIST, Bangladesh

Assoc. Prof. Maj Md. Manwarul Haq
MIST, Bangladesh

Md Moslem Uddin
Chief Librarian, MIST, Bangladesh

ADVISORY BOARD MEMBERS

Prof. Chanchal Roy
University of Saskatchewan, Canada

Prof. Mahmud Ashraf
Deakin University, Australia

Prof. Daili Feng
University of Science and Technology Beijing, China

Assoc. Prof. A. K. M. Najmul Islam
LUT University, Finland

Prof. Arnab Roy
Indian Institute of Technology (IIT) Kharagpur, India

Prof. Ahmad Faris Ismail
International Islamic University Malaysia (IIUM), Malaysia

Dr. Bhuiyan Shameem Mahmood Ebna Hai
Helmut Schmidt University, Germany

Prof. Md Shahidul Islam
Khulna University of Engineering & Technology, Bangladesh

Prof. Reza Nakahie Jazar
RMIT University, Australia

Prof. Md Azizur Rahman
Texas A&M University, Qatar

Prof. Bashir Ahmmad Arima
Yamagata University, Japan

Prof. Kobayahsi Kensei
Yokohama National University, Japan

Prof. Mohammad Kaykobad
BUET, Bangladesh

Prof. Sunil S. Chirayath
Texas A&M University, USA

Prof. Md Hadiuzzaman
BUET, Bangladesh

Prof. Rezaul Karim Begg
Victoria University, Australia

DISCLAIMER

The analysis, opinions, and conclusions expressed or implied in this Journal are those of the authors and do not necessarily represent the views of the MIST, Bangladesh Armed Forces, or any other agencies of Bangladesh Government. Statements of fact or opinion appearing in MIJST Journal are solely those of the authors and do not imply endorsement by the editors or publisher.

ISSN: 2224-2007
E-ISSN: 2707-7365

QUERIES ON SUBMISSION

For any query on submission the author(s) should contact: MIST, Mirpur Cantonment, Dhaka-1216, Bangladesh; Tel: 88 02 8034194, FAX: 88 02 9011311, email: *mijst@mist.ac.bd*. For detailed information on submission of articles, the author(s) should refer to the Call for Papers and About MIJST at the back cover of the MIJST Journal. Authors must browse MIJST website through the journal link (*https://mijst.mist.ac.bd/mijst*) for electronic submission of their manuscripts.

PUBLISHER

Military Institute of Science and Technology (MIST), Dhaka, Bangladesh

DESIGN AND PRINTING

Research and Development Wing
Military Institute of Science and Technology (MIST)
Dhaka, Bangladesh

FOREWORD

Bismillahir Rahmanir Rahim

MIST International Journal of Science and Technology (MIJST) series aims at providing a forum for scientists, engineers, researchers, educators and professionals from around the world for sharing the research findings using the state-of-art technologies in their respective fields. Through its quality and timely publication, MIJST has made its mark as a quality journal at home and abroad.

It was pleasure to endorse a series of reform drives in 2021 by MIJST Board aimed at meeting all the requirements of Scopus and WoS indexing by MIJST. With the restructured Journal and the Advisory Boards, comprising prominent researchers from the entire globe, I firmly believe that MIJST will be capable of achieving its desired goal of getting enlisted in Scopus and WoS. I would like to welcome all the new members of the restructured Journal and the Advisory Boards and wish to have their meaningful cooperation and guidance to steer MIJST through a successful journey to achieving global recognition. At the same time I would like to thank all the valued authors who have contributed to this issue of the MIJST. Special thanks and gratitude are also due to all the learned reviewers of the issue for their valuable contributions towards enhancing the quality of the articles. I would like to also extend my whole-hearted thanks to the entire MIJST team for the timely publication of the current as well as all the previous issues of MIJST.

I wish continued success of MIJST in the years to come!

Major General Md Wahid-Uz-Zaman, BSP, ndc, aowc, psc, te
Commandant, MIST, Bangladesh
Chief Patron, MIJST, Bangladesh

EDITORIAL

It is a matter of great satisfaction that the 2nd issue (December 2021) has been published on schedule thanks to the commitment and concerted effort made by the authors, reviewers, editorial and production teams despite the continuation of the COVID-19 pandemic globally.

I am very pleased to inform you that apart from making the MIST International Journal of Science and Technology (MIJST) visible and indexed through Google Scholar, DOI Crossref., Microsoft Academic Search, Semantic Scholar, Publons, Creative Common, BanglaJOL, and Open Journal system within a timeframe less than two years, we have completely revitalised the Journal's editorial and advisory teams. By visiting the Journal's website, you would be able to see the dynamic makeup of the new Editorial and Advisory Board members who are truly world class experts in their respective fields representing over 22 countries from all continents. With this new energetic team, we are now more confident to materialise the roadmap for getting the Journal to be indexed in SCOPUS, Web of Science (WoS), Emerging Source Citation Indexing (ESCI) by Thomson Reuters/Clarivate Analytics, and Directory of Open Access Journals (DOAJ) within the shortest possible time.

We urge you to submit your scholarly unpublished, original, and innovative contributions from any branch of science, engineering, technology, and related fields to our Journal. All submitted contributions will go through a double-blind peer-review process with effective feedback as we are committed to publishing high quality original and innovative work.

The December issue includes five original research articles focussing on innovative autonomous braking system for automotive application, emergency cooling of the state-of-the-art VVER-1200 nuclear reactor, fully developed channel flow prediction, urban fabric design for seaport from Grasshopper perspective, and the design of low head vortex turbine for mini hydropower plant. These articles deal with the real-world problems.

Finally, I express my heartfelt gratitude and thanks to the Chief Patron, Executive Editor, Associate Editors, Reviewers, Editorial and Advisory Board members, proof-readers, and web production consultant for their wholehearted support, commitment, hard work, and passion for this journal. I call upon you to promote the MIST International Journal of Science and Technology (MIJST) among colleagues, research scholars, and library liaison officers.

Your valued feedback, suggestion, and advice for the advancement of this journal are cordially welcome. Please feel free to contact me via telephone +61 3 99256103 and/or email: firoz.alam@rmit.edu.au; mijst@mist.ac.bd.

Sincerely,

Prof. Dr. Firoz Alam
Editor in Chief

INDEX

MIJST
MIST International Journal of Science and Technology

Autonomous Braking System: for Automobile Use

Ataur Rahman[1*], Sany Izan Ihsan[2]

Department of Mechanical Engineering, Kulliyyah of Engineering, International Islamic University Malaysia (IIUM), Kuala Lumpur, Malaysia

Emails: *[*1]arat@iium.edu.my; [2]sihsan@iium.edu.my*

ARTICLE INFO

Article History:

Received: 07th October 2021
Revised: 23rd November 2021
Accepted: 24th November 2021
Published: 23rd December 2021

Keywords:

Autonomous braking
Advanced vehicle
Adaptive neuro-fuzzy interference
Genetic algorithm
Sensors bank
Uncertainty

ABSTRACT

Road fatality and injury are a worldwide issue in the transportation industry. Road traffic accidents are becoming increasingly significant due to higher mortality, injury, and disability across the world, particularly in developing and transitional economies. Eighty-five percent of the total road traffic fatalities occur in developing nations, with Asia-Pacific accounting for roughly half of them. A variety of factors influence road safety, including technological, physical, social, and cultural factors. The purpose of this research was to design an autonomous braking system (AuBS). Using the Adaptive Neuro-Fuzzy Intelligent System (ANFIS), a DC motor, sensors, and SAuBS have been developed to customize the traditional hydraulic braking system. The genetic algorithm has been developed to simulate the fundamental characteristics of the automotive braking system. The AuBS system goal is to slow the car without the driver's help infrequent braking when the vehicle is moving at slower speeds. When the ANFIS performance is compared to that of the AuBS model, it is discovered that the ANFIS performs roughly 15% better.

1. INTRODUCTION

In the transportation sector, road fatality and injury are known global issues. Major research on the topic of road traffic accidents and fatalities has been emphasized by the World Bank, World Health Organization (WHO), Transport Research Laboratory (TRL), and others. Road traffic accidents are becoming increasingly important as a source of death, injury, and disability all across the world, particularly in developing and transitional economies (Mittal, 2008). Road traffic accidents entail not only enormous financial losses, but also severe physical and mental anguish for people, families, and businesses. According to WHO figures, road traffic accidents account for 75% of deaths in developing nations, despite the fact that they own only 32% of the world's vehicles. Road traffic accidents are expected to cost the world economy USD 518 billion each year.

Another major source of road traffic accidents and deaths in the country is the country's rapid expansion in the number of automobiles. Accidents happen because of the faults of drivers and other road users, or because of the faults of the vehicle. Human failure is caused by the driver's or the victim's guilt, alcoholic intoxication, exhaustion, irresponsible driving and not obeying the rules of the road, and ignorance of road safety, which result in an accident and death (Friduly, 1999).

The frightening of traffic accidents is a source of considerable concern for all of us. Eighty-five percent of road traffic deaths occur in developing nations, with Asia-Pacific accounting for roughly half of them. According to Anbalagan and Suyambukanni (2010), India accounts for around 10% of all road traffic deaths worldwide. Accidents on the road are unforeseeable, but they are not unavoidable. Road safety is complicated by a number of aspects, including technological and physical, as well as social and cultural (Hassen *et al.*, 2011).

In their study, the authors (Breuer *et al.*, 2007) found that late and untimely driver intervention in braking, as well as insufficient braking torque obtained in emergency scenarios, are among the leading causes of road accidents.

Late braking was found to be caused by driver irresponsibility and human error by the European New Car Assessment Program (Euro NCAP) (Pain *et al.*, 2011). Studies were conducted in the domain of active vehicle safety to lessen these issues, which led to the introduction of Advanced Driver Assistance Systems (ADAS) (Hamid *et al.*, 2016). To address these difficulties, researchers in the field of vehicle active safety conducted research, which led to the creation of Advanced Driver Assistance Systems (ADAS). Collision avoidance (Hamid *et al.*, 2017), blind-spot monitoring, and automated emergency braking (AEB) (Fildes *et al.*, 2015) are examples of notable ADAS

applications. AEB is an ADAS feature that works autonomously, without the need for human interaction, to lessen the chance of a collision in dangerous situations by applying braking torque. Volvo City Safety (Distner *et al.*, 2009), VOLKS WAGON Front Assist (Berger *et al.*, 2015), and the 2010 Mercedes-Benz PRE-SAFER Brake (Zwahlen *et al.*, 2016) are three AEBs that have been introduced on the road in the last five years.

Despite the vast number of commercial AEB products, crash events have occurred when the distance between the vehicle to vehicle is too near (Hong *et al.*, 2013). To avoid this issue, an AEB system that considers and maintains a safe distance from the point of impact should be developed (Rahman *et al.*, 2018). The ASEAN New Car Assessment Program (ASEAN NCAP) mentioned the AEB as a requirement in its new grading protocols for 2017-2020 (Asean nCAP, 2020).

Over time, innovators have added new features to the brake system with the goal of easing driving environments by improving braking performance. The evolution of brakes has been impressive, and it has incorporated many technological breakthroughs over the years (Rahman *et al.*, 2018).

Nowadays, assist systems have diffused from high-end to low-cost automobiles, and they are known by various names such as advanced safety assist (ASA), smart sensing, advanced driver assist system (ADAS), and so on. As a result, automatic emergency braking (AEB) evolves, in which the car automatically applies brakes in a dangerous scenario without the assistance of the driver. The system integrates an ultrasonic sensor with a controller to identify if the vehicle is within a specified range. If the driver looks to be ignorant of the situation, the system will activate AEB to reduce the risk of accidents (Zwablen *et al.*, 2016).

This research aims to present a fundamental autonomous braking system with the existing hydro-mechanical braking system, in which the brake pedal simply engages with an electromagnetic system based on the signals of the accelerator pedal sensor and the wheel speed sensor. The ANFIS controller has been proposed to control the power flow to the electromagnetic system since the fluctuating velocity necessitated varying pressure to maintain the vehicle's decelerating distance to a full stop.

2. MATERIALS AND METHODS

The development of the AuBS was carried out following the flow chart as shown in Figure 1. The dc servo-motor actuates the master cylinder to create the appropriate brake hydraulic pressure from the master cylinder (MC) for the creation of braking force at the wheel-calipers, as shown in the diagram. Hydraulic braking mechanism, dc servo-motor, ANFIS controller, wheel speed and ultrasonic sensors, and a dc power source are the main components of the AuBS.

2.1 Braking System Architecture

Figure 2 depicts an AI-based IoT-controlled DC motor-powered autonomous electro-hydraulic braking system (AEHBS). The DC motor supports the brake pedal force in this system, with the wheel speed sensor, brake controller, and proportional valve controlling the total system.

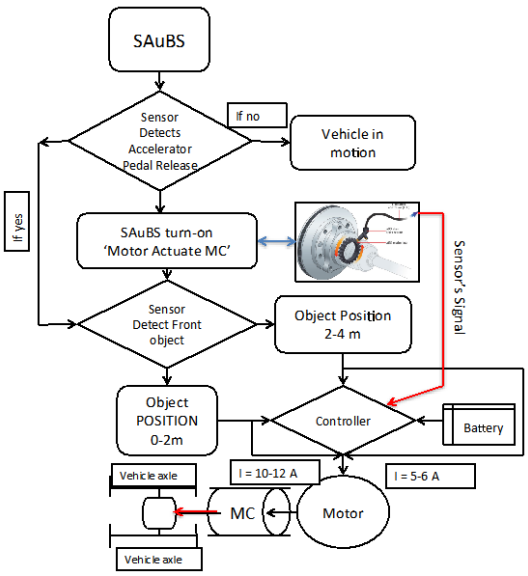

Figure 1: Flow of action of S AuBS

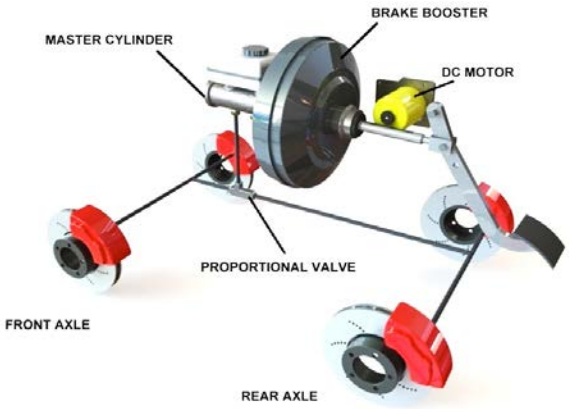

Figure 2: Architecture of Autonomous braking system

Performance characteristics of a road vehicle refer to its capability to decelerate and full-stop in a shorter distance. The braking torque required to decelerate or stop the vehicle can be estimated [9,10]:

$$T_{b(f)} = \frac{\mu_{bp} \times x_f \times P_{mc} \theta}{3} \quad (1)$$

$$T_{b(r)} = \frac{\mu_{bp} \times x_r \times P_{mc} \theta}{3} (r_o^3 - r_i^3) \quad (2)$$

where, μ_{bp} is the brake pad friction coefficient, T_b braking torque of the rotor, Nm, P_{mc} master cylinder pressure, θ is the angular position of the brake pad from the centre of the rotor, T_t traction torque of the vehicle, Nm, x_r is the percentage of P_{mc} to the front axle and x_r is the percentage of P_{mc} to rear axle. The suffix f and r represent front and rear axle and o and i indicate the outer radius and inner radius of the brake pad from the centre of the braking rotor.

a. Rotor barking torque to decelerate the car,

$$T_{b(f)}(t) + T_{b(r)}(t) < T_x \quad (3)$$

b. Rotor braking torque to a full stop the car,

$$T_{b(f)}(t) + T_{b(r)}(t) \geq T_x \quad (4)$$

where, T_x is the traction torque, Nm.

2.2 Generic Form Algorithm for the AuBS

The braking power of the braking system in this study has been assigned based on the signal of the wheel speed sensor, ultrasonic sensor and accelerator sensor. The vehicle starts to decelerate when the accelerator pedal releases and the master cylinder starts to develop the braking pressure for the braking devices (either disk or drum braking). The braking devices develop the actuation force which causes the development of braking force at the brake pad and the vehicle decelerates or full stop. Based on the condition of the braking force development, the genetic algorithm has been developed, $B_f \geq 0$. Braking force is subjected to instantaneous signal of:

i. Wheel speed sensor,

$$wss\ (t) = \dot{x}\ ,\ 0 \leq \dot{x}\ \leq 120(km/h) \quad (5)$$

ii. Ultrasonic sensor signal,

$$us\ (t) = x\ ,\ 2 \leq x \leq 5\ (m) \quad (6)$$

$$Rotor\ speed, M_r\ (t) = \oint (I_b) \quad (7)$$

$$Braking\ force, B_f = \oint (rpm_{wss}) \quad (8)$$

$$Error, e = M_r - M_a \quad (9)$$

$$Rate\ of\ error, \dot{e} = \frac{d}{dt}\ [M_r - M_a] \quad (10)$$

where, $\dot{x}$ is the speed of the wheel, km/h, x displacement based on the signal of ultrasonic sensor, m , e error between rotor rpm and wheel actual rpm, $\dot{e}$ is the rate of error, M_r rotor rpm, M_a actual rpm.

Figure 3 shows the controlling action of the AuBS using ANFIS to decelerate the vehicle starts when the driver to lift-up foot from the acceleration pedal. The system then starts working with the input from the ultrasonic sensor and wheel speed sensor, send to the controller, which controls the power flow to the motor to actuate the MC in the development of hydraulic pressure to decelerate or fully stop the car without the driver any effort. When the car is at a higher or cruising speed, however, this system will not be useful to fully stop the vehicle.

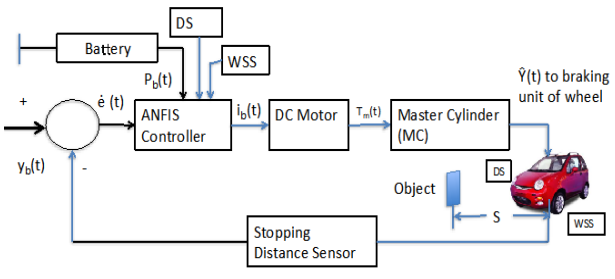

P_B (t) – Instantaneous battery power to motor, i_b(t)- battery current, T_m(t)-motor torque, Ŷ(t)=hydraulic pressure to braking unit of the wheel, y_b(t) – braking unit pressure, WSS – wheel speed sensor, DS-distance sensor, S-stopping distance.

Figure 3: Basic block diagram of a closed-loop vehicle braking system

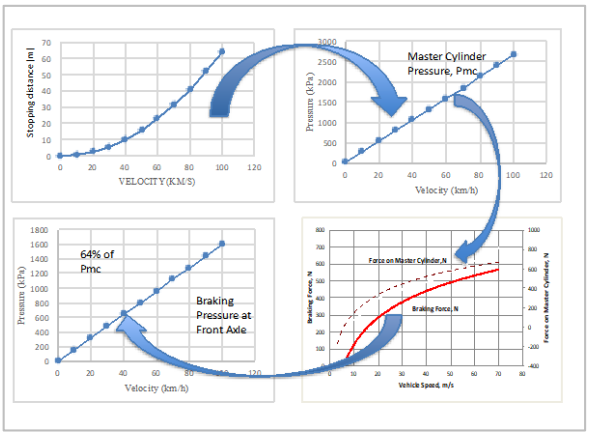

Figure 4: Fundamental of braking system

Figure 4 depicts the basic braking characteristics that must be met by the vehicle's braking system during deceleration or full stop. It is also critical to avoid a vehicle collision. The diagram depicts the vehicle's safe braking distance at various speeds, as well as the required force on the MC and hydraulic pressure on the axles. The related force on the MC will be roughly $510N$ if the vehicle's safe stopping distance is $30\,m$ at $40\,km/h$, allowing the hydraulic pressure to rise to $1100\,kPa$. As a result, the hydraulic pressure at the front axle will increase by around 64%. A pressure of $620\,kPa$ is ($620\,kPa$).

3. CONTROL STRATEGY OF SAuBS

An adaptive neuro-fuzzy inference system (ANFIS) is a type of artificial neural network that uses the Takagi–Sugeno fuzzy inference system. It combines neural networks and fuzzy logic concepts, allowing it to capture the advantages of both in a single framework. Its inference system is made up of a set of fuzzy IF–THEN rules with the capacity to approximate nonlinear functions through learning. The best parameters obtained by a genetic algorithm can be used to make the ANFIS more efficient and ideal.

3.1 ANFIS Structure

Layer 1 The inputs to the nods in the first layer are the fuzzy sets of the ANFIS. Every node in this layer is an adaptive node. The layer is connected between the input terminal and its corresponding membership function nodes.

Layer 2: This layer's nodes are all circle nodes labelled Π It multiplies the input signals and sends the final result out. For example,

$$w_i = \mu a_i(x) \times \mu b_i(y), i = 1, 2; \quad (11)$$

where, μa_i is the membership function of linguistic variable a and μb_i is the membership function of variable b, a_i is the linguistic level (very small, VL, small L, M medium, H high and XH extreme high) and similarly for b_i (VL, L, M, H, and XH). Each node output represents the firing strength of a rule.

Level 3: N is the label for each node in this layer is assigned by N. The i-th node determines the ratio of the firing strength of the i-th rule to the total firing strength of all rules:

$$\bar{w}_i = \frac{w_i}{w_1+w_2}, i = 1,2; \quad (12)$$

Here, $\bar{w}$ is the normalized fring strength of rule i.

Layer 4: This layer node is an adaptive node, connected to the corresponding normalized node in the previous layer, and receive inputs from x and y. Each node in this layer is a local linear model of the Sugeno fuzzy system; integration of outputs of all local linear model yields predicted output:

$$\bar{w}_i p_i = \bar{w}_i(r_0 + m_r x + n_i y) \quad (13)$$

Layer 5: The single node in the layer is a fixed mode levelled $\sum$, which computes the overall output as the summation of all incoming signals:

$$P = \frac{w_1 P_1 + w_2 p_2 + \cdots + w_5 p_5}{w_1+w_2+\cdots+w_7} = \bar{w}_1 p_1 + \bar{w}_2 p_2 + \cdots + \bar{w}_5 p_5 \quad (14)$$

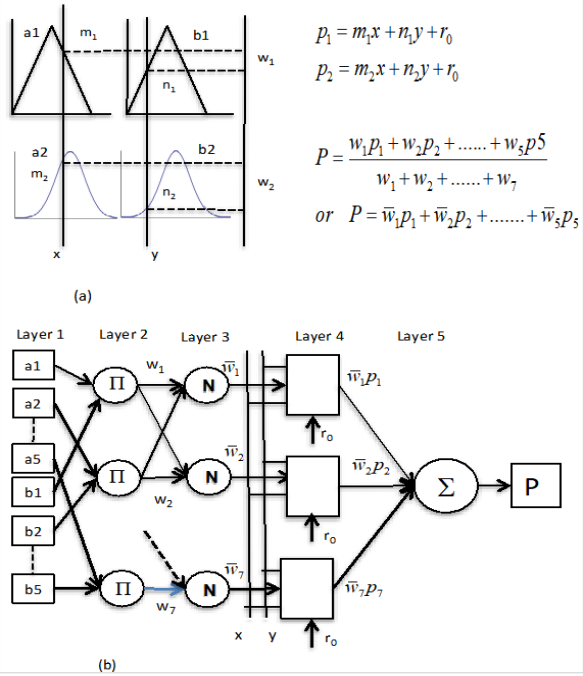

Figure 5: ANFIS model classification

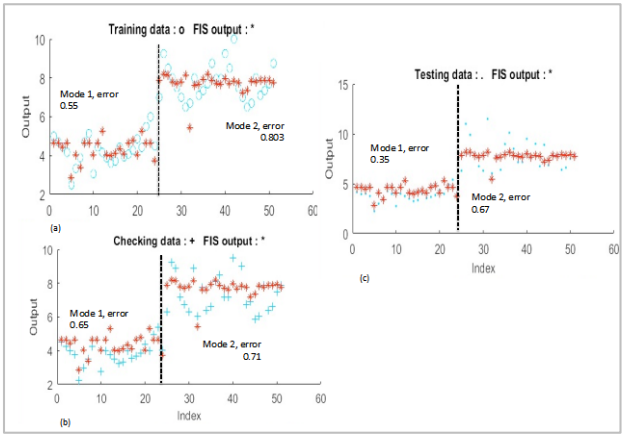

Figure 6: Theoretical ANFIS model performance

3.2 Training, Checking and Testing of the ANFIS model

The ANFIS model is trained, checked, and tested using the MATLAB software program, which allows for easy manipulation of the model's parameters and variables. The system receives the entire set of data on the vehicle's motor speed, sinkage, and power requirement, is divided into three parts:

i. Training data, which made up 69.8% of the total 102 data set, enabled so-called "learning with a supervisor," in which the network's output is known ahead of time for proper inputs. The least error of training data as shown in Figure 6 (a) is 0.55 for mode 1 (deceleration), 0.803 for mode 2 (full stop), and 0.69 for overall.

ii. Checking data, which is primarily intended to prevent over-fitting of training data. In each training period, the ANFIS model monitors the value of the checking error. As illustrated in Figure 6 (b), the overall error is 0.83. The checking data makes up 50% of the total data set. The checking data has been made using MATLAB Simulink.

iii. We used testing data to evaluate the ANFIS model. The output of the ANFIS model is compared to known values in order to discover the least amount of inaccuracy possible. The smallest inaccuracy was 0.23, as shown in Figure 6(c). Testing data accounted for nearly 50% of the total data set. Data for testing was gathered from a field experiment.

Figure 4 also shows that the fuzzy interference data is more correlated compared to the training data and checking data. This is because of the ANFIS interpretation capability and the ease of encoding a priori knowledge.

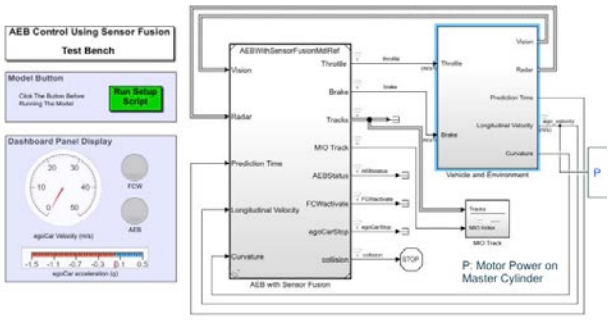

Figure 7: ANFIS trained AEM model

A MATLAB ANFIS controller Simulink model has been designed to optimize the braking pressure of the master cylinder to deceleration/full stop of the vehicle. The working range for the controller has shown in Table 1 which has been identified from the ANFIS MATLAB model.

4. CASE STUDY: VEHICLE IN PEDESTRIAN

4.1 AEB Model Study- Pedestrian Crossing

The Autonomous Emergency Braking (AEB) technology assists drivers by providing sufficient braking force to avoid a crash. This system uses an obstacle positioning sensor and a speed sensor, and the system's output is braking force, which can come from the action motor power that applies force on the master cylinder which produces the braking pressure. The Adaptive Neuro-Fuzzy

Inference System (ANFIS) is a technology that may be used to train a controller that mimics human behavior using current experimental data. When a data set is entered into ANFIS, membership functions are generated, which are then trained into a set of rules that can be satisfied. ANFIS will train an AEB controller in this project, resulting in a system that can autonomously mitigate any road collision. Figure 7 shows the ANFIS Matlab model to simulate the optimum braking system effective parameters with trained AEM model data.

Table 1
Working condition for AuBS

Vehicle Dynamic mode	Distance between vehicle (m)		Force applied at MC (kN)
	Front	Side	
Power brake	$2.5 - 2.0$	0.0	$0.9 - 1.7$
Deceleration	$3.5 - 2.5$	$0.0 - 0.5$	$0.0 - 0.9$
Cruising	$4.0 - 3.5$	$0.51 - above$	0.0

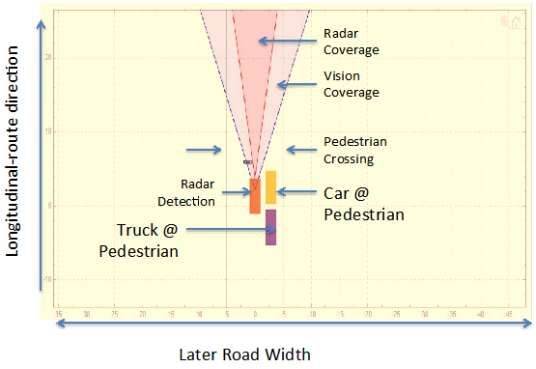

Figure 8: Pedestrian crossing

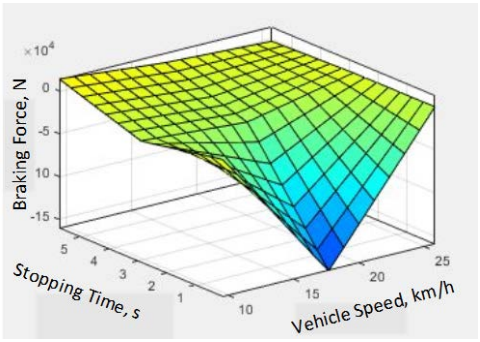

Figure 9: ANFIS simulation result for pedestrian

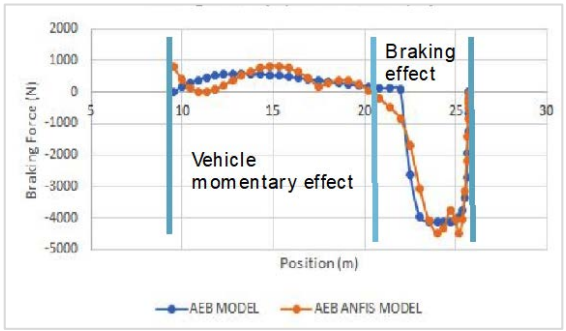

Figure 10: Comparison of ANFIS model with AEB model

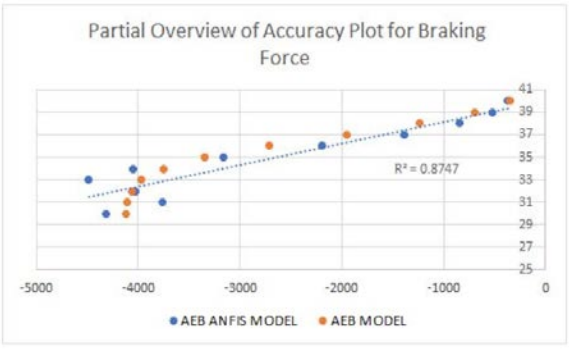

Figure 11: ANFIS result is verified with the AEB model result

The pedestrian crossing and the location of the car recognized by the RADAR SENSOR are visualized in Figure 8. Figure 9 shows the ANFIS model is being simulated with radar sensor input and compared with the AEM model in Figure 10. In terms of generating braking force, Figure 9 shows how the ANFIS model outperforms the AEB model. The ANFIS controller will activate the braking system just before the crossing, causing the automobile to slow down or stop completely. Figure 11 depicts the 88 percent discrepancy between the AEM and ANFIS results.

6. AEB MODEL TESTING - EXPERIMENTALLY

A laboratory ¼ scale prototype of AuBS as shown in Figure 12, was constructed using a typical scouter braking system, which includes the master cylinder, brake pad, brake callipers, and brake tube (Figure 12). The performance of the prototype has been conducted using a $155kg$ load, road adhesion, μ_p = 0.6, frictional coefficient of brake pad, $\mu bp = 0.46$, and master cylinder bore of 2.85 cm.

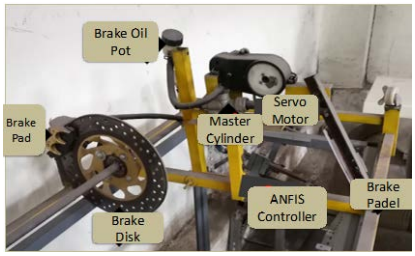

Figure 12: A laboratory scale AuBS

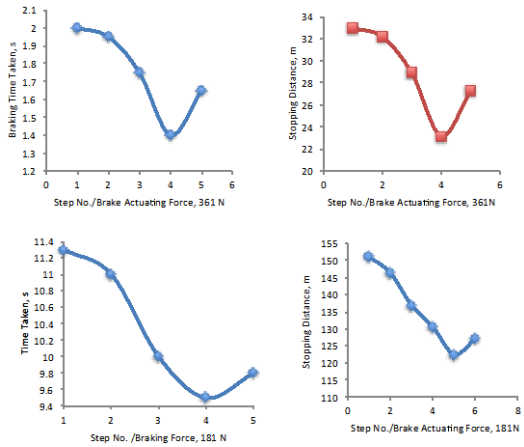

Figure 13: ANFIS controlled laboratory scale AuBS

The experimental result of the laboratory scale AuBS controller equipped brake system is shown in Figure 12. The servo-motor applied forces of $181\ N$ and $361\ N$ on the MC were used in the testing. The vehicle's stopping distance was found to be $23\ m$ at time 1.4 s for the applied force $361\ N$, while its braking distance was found to be $122\ m$ at time 9.5 s for the braking force of $181\ N$.

7. CONCLUSIONS

- Semi-Autonomous Braking System (AuBS) can be used as a stepping stone for the vehicle's braking system during traffic congestion to reduce the driver's input.
- ANFIS controlled braking system is more efficient than a conventional braking system at decelerating or fully stopping the vehicle without the need of the driver's support.
- Servo motor speed is inefficient to quickly control the vehicle, especially in GO/STOP mode dynamics and keep the vehicle in safe mode.
- AuBS adds value to the existing conventional braking system to control the vehicle based on the response of ultrasonic and photosensors in pedestrian crossings and slow-moving traffic.
- To justify the AuBS performance, more research is needed in the lab and the field with a full-scale AuBS model.

ACKNOWLEDGEMENTS

Authors would like to express their gratitude to the Dept. of Mechanical Engineering, IIUM, Kuala Lumpur, Malaysia. They also would like to thank the anonymous reviewers and editorial board members of MIJST for insightful comments and suggestions.

REFERENCES

Anbalagan P & Suyambukanni N, “Non-Motorized Transport (with special reference to Bicycles in Chennai City)” Indian Journal of Transport Management, Oct-Dec 2010, Vol. 34(4), pp 273-284.

ASEAN NCAP, “Asean ncap new rating protocols for 2017-2020 - the new car assessment program for southeast asia,” http://aseancap.org, accessed: 2017.08.26.

Berger, D. Block, S. Heeren, C. Hons, S. Kuhnel, A. Leschke, D. Plotnikov, and B. Rumpe, “Simulations on consumer tests: A systematic evaluation approach in an industrial case study,” IEEE Intelligent Transportation Systems Magazine, vol. 7, no. 4, pp. 24–36, 2015.

Breuer, A. Faulhaber, P. Frank, and S. Gleissner, “Realworldsafety benefits of brake assistance systems,” in 20th International Technical Conference on the Enhanced Safety of Vehicles (ESV), no. 07-0103, 2007.

Distner, M. Bengtsson, T. Broberg, and L. Jakobsson, “City safetya system addressing rear-end collisions at low speeds,” in Proc. 21st International Technical Conference on the Enhanced Safety of Vehicles, no. 09-0371, 2009.

Fildes, M. Keall, N. Bos, A. Lie, Y. Page, C. Pastor, L. Pennisi, M. Rizzi, P. Thomas, and C. Tingvall, “Effectiveness of low speed au- tonomous emergency braking in real-world rear-end crashes,” Accident Analysis & Prevention, vol. 81, pp. 24–29, 2015.

Fridulv Sagberg (1999), „Road accidents caused by drivers falling asleep“, Accid. Anal. Prev., Vol. 31, pp.639-649.

Hassen, A., Godesso, A., Abebe, L., and Girma, E. (2011). Risky driving behaviours for road traffic accident among drivers in Mekele city, Northern Ethiopia. Research Notes, 4, 535.

Hamid, K. Pushkin, H. Zamzuri, D. Gueraiche, and M. A. A. Rahman, “Current collision mitigation technologies for advanced driver assistance systems–a survey,” PERINTIS eJournal, vol. 6, no. 2, 2016.

Hamid, M. H. M. Ariff, H. Zamzuri, Y. Saito, M. A. Zakaria, M. A. A. Rahman, and P. Raksincharoensak, “Piecewise trajectory replanner for highway collision avoidance systems with safe-distance based threat assessment strategy and nonlinear model predictive control,” Journal of Intelligent & Robotic Systems, pp. 1–23, 2017.

Mittal, N. SIMBA Project, “Policies and Programs for road safety in developing India”, Division of Environment and Road Traffic safety, Central Road Research Institute, New Delhi, India, 2008.

Paine, D. Paine, C. Newland, and S. Worden, “Encouraging safer vehicles through enhancements to the ncap rating system,” in 22nd International Technical Conference on the Enhanced Safety of Vehicles (ESV), no. 11-0107, 2011.

Rahman, A. and Mohamad Amsyar (2018) DC motor amplified mechanical-hydraulic braking system for passenger car. Journal of Applied Science, Vol.18(2): pp.56-64.

Rahman, Mohiuddin AKM and Ahsan Sakif (2018) Development of electro-hydro automatic parking braking system: Automotive use. International Journal of Engineering and Technology., Vol.7(6S), 264-269.

Rahman, A. and Mohamad Amsyar (2018) DC motor amplified mechanical-hydraulic braking system for passenger car. Journal of Applied Science, Vol.18(2): pp.56-64.

Rahman, A, Nurul Hasan, Mohd Zaki (2020) Modelling and Validation of Electric Vehicle Drive Line Architectureusing Bond Graph. TEST Engineering and Management, Vol.82 (Jan-Feb, 2020), pp.15154-1516.

Zwahlen, C. Jackowski, and M. Pfa¨ffli, “Sleepiness, driving, and motor vehicle accidents: A questionnaire-based survey,” Journal of forensic and legal medicine, vol. 44, pp. 183–187, 2016.

MIJST
MIST International Journal of Science and Technology

Effect of Boric Acid Solubility in Steam on the Process of Mass Transfer during Emergency Cooling of VVER-1200 Nuclear Reactor

Md. Rezouanul Kabir Hridoy[1*], Morozov A.V.[2], Md Saif Kabir[3]

Department of Nuclear Physics and Engineering, National Research Nuclear University (MEPhI), Russia

Emails: *[1]rezouanul@oiate.ru; [2]morozovandrey.email@gmail.com ; [3]mdsaifkabir@oiate.ru

ARTICLE INFO

Article History:

Received: 21st August 2021
Revised: 15th November 2021
Accepted: 16th November 2021
Published: 23rd Decemer 2021

Keywords:

VVER-1200
Crystallization
Hydroaccumulator-1, 2
Boric Acid
Reactor Core

ABSTRACT

The mechanisms of boric acid mass transfer in a VVER-1200 reactor core are studied in this work in the event of a major circulatory pipeline rupture and loss of all AC power. The VVER-1200's passive core cooling technology is made up of two levels of hydro accumulators. They use boric acid solution with a concentration of 16 g H3BO3/kg H2O to control the reactivity. Because of the long duration of the accident process, the coolant with high boron content starts boiling and steam with low concentration of boric acid departs the core. So, conditions could arise in the reactor for possible accumulation and subsequent crystallization of boric acid, causing the core heat removal process to deteriorate. Calculations were carried out to estimate the likelihood of H3BO3 build-up and subsequent crystallization in the core of the VVER reactor. According to the calculations, during emergency the boric acid concentration in the reactor core is 0.153 kg/ kg and 0.158 kg/kg in both the events of solubility of steam and without solubility of steam respectively and it does not exceed the solubility limit which is about 0.415 kg/kg at water saturation temperature. No precipitation of boric acid occurs within this time during the whole emergency process. Therefore, findings of the study can be used to verify whether the process of decay heat removal is affected or not.

1. INTRODUCTION

The majority pressing issues that need to be addressed to the industry of nuclear power today are for ensuring the safety of new electricity plants with nuclear reactors. The passive safety system (PSS) functioning ensures reactor unit safety during loss of coolant accident (LOCA) in the water-water energetic reactor (VVER-1200) reactor project. PSS removes heat through the core by supplying solution of boric acid having concentration of 16g/kg to the reactor (Kalyakin *et al.*, 2003; Morozov *et al.*, 2009). Heat removal through fuel elements can deteriorate as a result of this and this can lead to a negative environmental effect. The review of potential incidents at nuclear power plant for an era of VVER fitted with passive protection systems would benefit greatly from the evaluation of boric acid removal from the core. Experiments have demonstrated that high amounts of boric acid can be achieved in the core simulator, resulting in its crystallization and disrupting coolant circulation. Droplet entrainment has also been found to cause the boric acid's concentration to rise in the core. In experiments which were carried out without a separator to prevent droplet entrainment, boric acid (H3BO3) concentration in the core simulator reached equilibrium below the saturation limit, and crystallization was not seen. This was due to the fact that steam took out the same amount of boric acid solution as vapour. Calculations and experiments revealed that the capturing of boric acid droplets was not as strong when pure water was used. This suggests that both H_3BO_3 and the presence of other impurities in water have a direct effect in the process of droplet entrainment. It necessitates theoretical and analytical research into the mechanism of boric acid droplet entrainment in the context of VVER in emergency boiling mode. The key goal of this study is to figure out how much boric acid droplets entrain during accident. The following issues must be resolved in order to accomplish this goal:

- Calculating and analysing of VVER reactor plant's mass transfer procedures (Morozov & Remizov, 2012).
- Calculating and analyzing the flow rates of Hydro-accumulator 2nd stage, PHRS and flow rates due to

droplet entrainment in emergency process (Kalyakin *et al.*, 2014)

2. THEORITICAL BACKGROUND

In emergency, there are two options for removing boric acid through the reactor core: In the steam-water mixture, through droplet entrainment and secondly, because of steam solvent ability.

A. Processes of droplet entrainment

In two-phase flow systems, understanding the conditions that contribute towards entrainment of a liquid film on the surface via a gas flow is crucial for mass and heat transfer operations. The onset of entrainment has a significant impact on the processes of mass, momentum and energy transmission (Ishii and Grolmes, 1975). In several methods, a gas flow can be entrained by a wavy liquid surface. The speed and distortion of wave crests are governed by hydrodynamic and surface forces. Under the horizontal air/water channel (HAWAC), Figure 1 demonstrates droplet production at wave crest in a slug flow situation (Vallée et al., 2008).

Figure 1: Droplets form at the peak of the wave (Vallée et al., 2008)

These pressures cause a severe distortion of the interface under certain conditions resulting in fragmentation of a section of a wave into numerous droplets. The surrounding flow pattern as well as the shape of the interface impact wave crests forces. Figure 2 depicts the four primary types of entrainment processes (Ishii & Grolmes, 1975). The turbulent gas flow shears the tops of big amplitude roll waves, away through wave crests in first kind (Hewitt and Hall-Taylor, 1970). The drag coefficient operating on the wave tops changes shape of the interface against the sustaining strain of liquid surface tension. The 2nd sort of entrainment occurs when a gas flow undercuts the liquid film (Hewitt & Hall-Taylor, 1970).

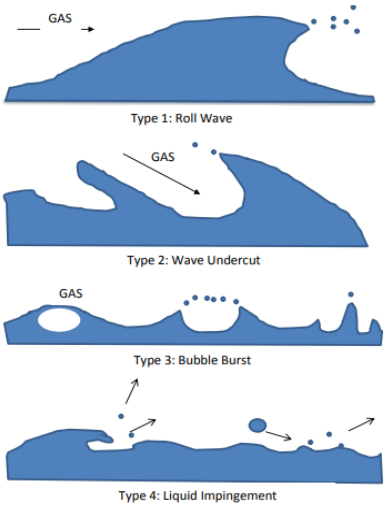

Figure 2: Different droplets entrainment mechanisms (Ishii & Grolmes, 1975)

The third type is associated with gas bubbles exploding (Newitt *et al.*, 1954). Liquid impingement droplets or bulk onto the film contact causes the fourth form of entrainment. This technique may create tiny droplets when roll-wave fronts advance. All of these scenarios should be covered by a universal droplet entrainment model.

B. Solubility of Boric Acid in Steam

In steam or supercritical water, all salts and oxides are relatively soluble. The degree of solubility is a complicated function of the substance's composition as well as the density and temperature of the water phase. At a constant temperature, solubility usually rises with density. The challenges caused by this solubility in the steam cycle are determined by cycle parameters and solute properties. However, deposits in the turbine typically extracted with steam from the steam generator chemicals, the most common of which are silica, Na-OH, Na2SO4 and copper oxides caused problems in conventional energy technology. Figure 3 demonstrates the concentration of steam solid in comparison to steam pressure.

The problem was solved principally by lowering the incoming amounts of chemicals in the unit and in case of silica by lowering its volatility by regulating the boiler's water alkalinity at its ideal level. The removal of water vapour from the transfer of substances might cause problems; therefore, it must be done mechanically using a device that monitors steam separation and draining. Chemistry of feed-water and boiler water has a direct impact on steam purity. Even at its finest, steam created during the boiling process is never totally clean. Solids deposition and corrosion in super-heaters and turbines are prevalent issues. Good steam chemistry management is critical in industrial units that do not have turbines. The term "carryover" refers to the process of solids being converted to steam. The following factors impact carryover:

- Almost all solids are soluble in steam. Solids become more soluble as boiler pressure increases.
- Even with the best steam separating devices, moisture droplets still enter the steam.
- Sulphate and chloride will enter steam as ammoniated salts.
- Carryover is increased by inadequate drum level management, poor drum structure or high particles accumulation in drum water. Dissolved solids still have a direct access to the steam system even if the drum is working effectively and limiting carryover.

In the event of an emergency, boric acid mass transfer must be investigated so that the risk pertaining to boric acid accumulation in the VVER core can be assessed. Whenever the main circulation pipeline ruptures in large loss of coolant accident, the water tanks hydroaccumulator-1 & hydroaccumulator-2 are activated to provide boric acid to the core (Morozov & Remizov, 2012a). In addition to boric acid, this accesses the reactor through water storage tanks and the activities of the passive heat removal system causing condensate to be dispersed into the core of the SGs

of three secondary exposed circuits about 1.5 hours shortly after the accident (Morozov & Remizov, 2012). In addition, there are two methods to address mass transfer of boric acid (Kalyakin *et al.*, 2014). Because the flow of boric acid into the downstream portion by operation of second stage hydro accumulator in a quantity suitable for natural convection, the condensation is mixed with the boric acid accreted in the first scenario at the bottom part of the reactor. A little amount of boric acid is added to the flow (Morozov & Remizov, 2012a).

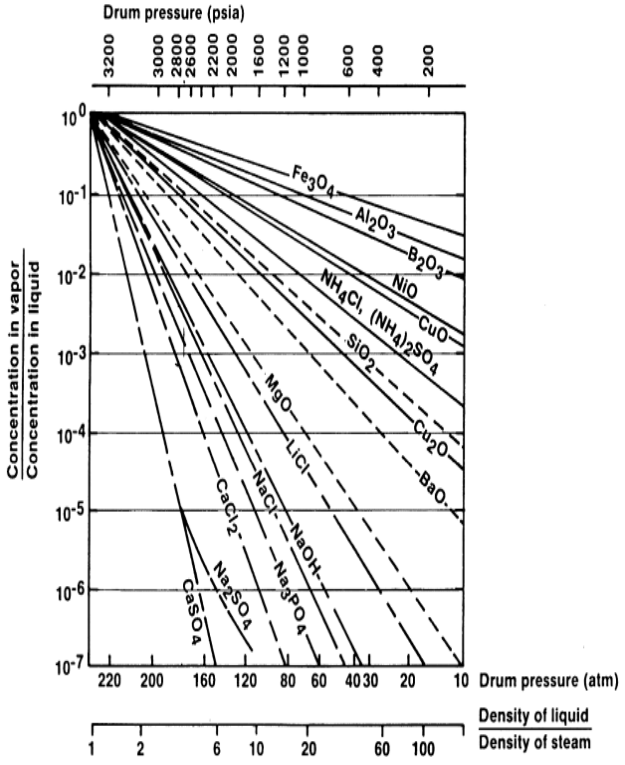

Figure 3: Concentration of Steam Solids vs. Steam Pressure

In the second scenario, condensate and HA-2-supplied boric acid do not combine. Then boric acid sinks towards the bottom region of the core as a result of increased density. Above this layer, condensate with a low acid content is collected. As a result, circumstances are produced for the concentration of boric acid to rise close to the lower part of the core for the acid to precipitate. Boric acid's density is determined by its concentration, as well as the density of water. Temperature affects the high concentrations in agreement with the commencement of the formation of crystals: an increase in temperature raises it dramatically, while a drop in temperature reduces it. Taking into account the creation of steam as a result of the coolant boiling in reactor, boric acid's concentration at the edge of the core should rise. Furthermore, the solubility in the reactor's volume might approach its maximum value.

The density of a boric acid solution is determined by the concentration of the acid and the density of the water (Schmal & Ivanov, 2015). The temperature affects the maximum concentration of boric acid solution that corresponds to the start of crystallization (Cohen, 1973): Temperature increase cause a rapid rise in the maximum concentration of boric acid solution, whereas temperature decrease lead to a reduction (Figure 4).

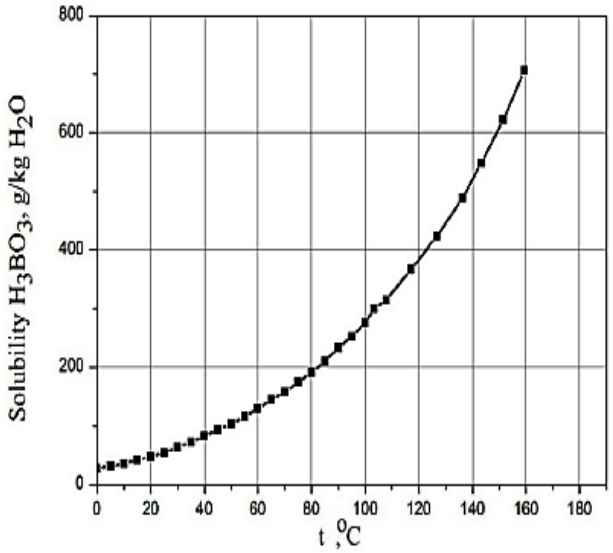

Figure 4: The diagram of the solubility of boric acid in water temperature (Cohen, 1973)

3. METHODOLOGY

A test facility was established at IPPE JSC (IPPE JSC is a research and development institute in the field of nuclear technology, located in Obninsk, Russia) to look into the mechanisms of boric acid mass transport. It is difficult to investigate these actual scenarios in nuclear power plant, so, this facility was used to obtain data.

A. Experimental Procedure

i. Test Facilities

The IPPE JSC test facility consists of a 14-liter solution preparation tank, an internal 27 mm stainless steel test section and a 2800 mm height, a steam condenser as well as a steam separator. The lower evaporative portion of the testing centre is heated by an adjustable heater. Insulated & heated technologies lines having shut-off valves link the facility's major equipment to one another (Hassan *et al.*, 2015). In the test section, the distance between the boiling water level and the steam extraction line in the VVER reactor and the low-level generator of the cold loop of the major circulatory pipeline corresponds to the height from the evaporative layer (Schmal & Ivanov, 2015).

The METRAN-150 gauge is used for measurement, display and transfer to pressure parameter control systems. A glass level gauge is used to measure the quantity of boric acid mixture in the test section. The temperature is monitored using K type cable temperature sensors with a diameter of around mm (measurement inaccuracy of 1 °C). The data collecting system's measurement channels have a 1 Hz sampling rate. The percentage of H3BO3 in the condensate specimens produced through condensing the steam created throughout the test specimen using boiling boric acid solution, is an essential measurable parameter in the tests.

ii. Experiment Steps

At the commencement of the test, the solution processing tank is full with the proper quantities of distilled water as well as dry powder H3BO3 to create a boric acid solution with a predetermined concentration. The solution was then

stirred using a mechanical device until the dry H3BO3 was completely dissolved which was observed through portholes in the tank. Nitrogen was subsequently transferred from gas cylinder to the solution preparation tank's top volume through the gas reducer. Temperature of the solution processing tank, the test section as well as the H3BO3 solution supply line was also elevated to the proper levels. Throughout the experiment, the required temperature should be maintained with a 1° C accuracy using a relay controller. After the preheating is completed, the valves in the H3BO3 solution supply line are released in order and the bottom half of the test section is loaded to the desired level using a boric acid solution with a concentration equivalent to that in the preparation tank. Simultaneously, a blow-off valve is opened to blast the steam-air combination out of the primary components into the environment, preventing the existence of a steam and air combination in test area. Power of the steam condenser is then controlled. The air fans are turned on to increase the power of the system.

The consistency of the quantity in the test section's pressure as well as the temperature of condensate at the output of the condenser is a condition for achieving the necessary value of the condensation power. After that, a 50ml sample of condensate is transported to the measurement containers at regular intervals throughout the experiment. The duration of condensate collected at the moment of sampling was used to establish the facility's actual evaporation power (Hassan *et al.*, 2015).

The calibration technique was accustomed to measure the boric acid's concentration in the samples after experiment was completed. Figure 5 depicts an organization of the test facility's primary equipment and Figure 6 depicts the facility's process flow chart.

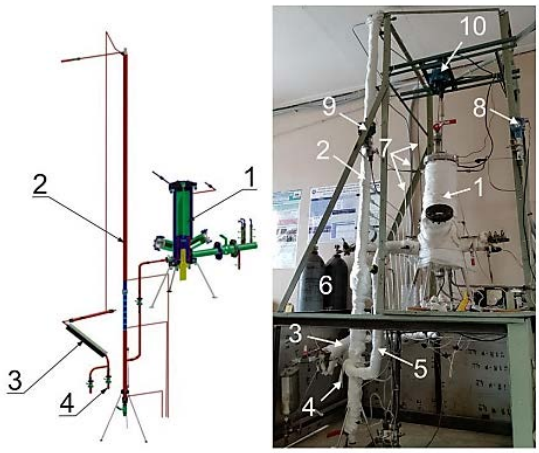

Figure 5: Arrangement of the test facility's major equipment (Hassan *et al.,* 2015): 1) solution preparation tank; 2) test section (TS); 3) condenser; 4) sampling; 5) line of H3BO3 solution supply; 6) a cylinder of the gas supply system; 7) steam extraction lines; 8, 9) pressure sensors; 10) mixing device

iii. Initial Data and Assumption

It is not feasible to compute droplet entrainment processes using dependencies in the early stages of an accident. As a result, the whole emergency procedure was separated into two sections throughout the computation analysis. Figure 7 (a) shows that the steam-water combination is splashed out in reactor volumes and contained in the pipeline in the early phase of an accident via the nuclear reactor core. The sprayed liquid water then rises over the hole of the reactor barrel, and then the steam-water mixture gets sprinkled from the core and goes into the reactor chamber. It finally goes to the containment since the pipeline is ruptured. This stage lasts about 7 hours. The residual energy release intensity decreases, the volume of the liquid steam is reduced and the boric acid solution level is set at MCP pipe height (second stage of the occurrence can be seen in Figure 7(b)).

A number of assumptions were assumed throughout the calculation, which is necessary owing to the difficulty of the processes happening in the circuit or the lack of data on the characteristics of boric acid solutions:

- During the computations, the reactor core volume and the reactor pressure chamber (RPC) volume had been allocated in the framework.
- Inacceptable conditions, the boric acid solution's thermal and physical properties – for example, density and viscosity should be assumed to be equal to the parameters of water.
- At the temperature of saturation, the core and RPC are both filled with all water.
- System pressure stays constant and is equivalent to 0.3 MPa
- All of the boric acid in the primary circuit, as well as the boric acid that enters the secondary circuit, is at saturation temperature.

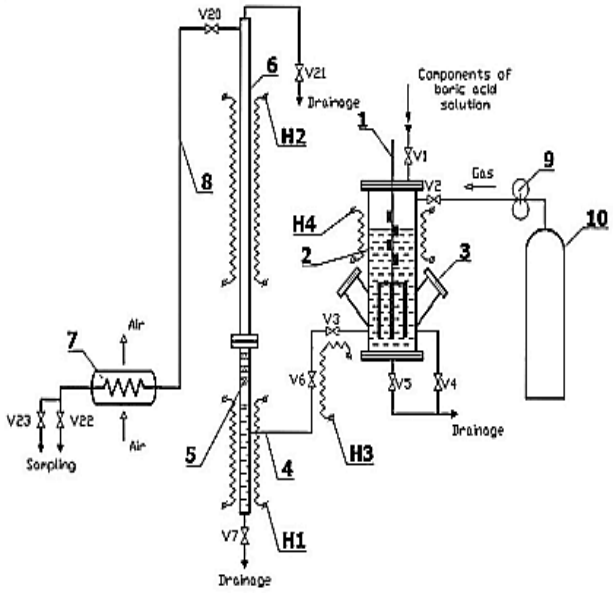

Figure 6: The test facility's process flow sheet. 1) apparatus for combining; 2) tank for preparing solutions; 3) port for observation; 4) H3BO3 solution supply line; 5) separator of steam; 6) test section; 7) condenser of steam; 8) steam extraction line; 9) reducer of gas; 10) cylinder of gas; H1-H4: electrical heaters in groups

At the time of mass transfer measuring, the rated capacity of the reactor was assumed to be $3.2 \times 109\ W$ (Kopytov *et*

al., 2009). The parameters of the accumulators of the passive flood of HA-2 were used as the starting point for the calculations (Morozov & Remizov, 2012b).

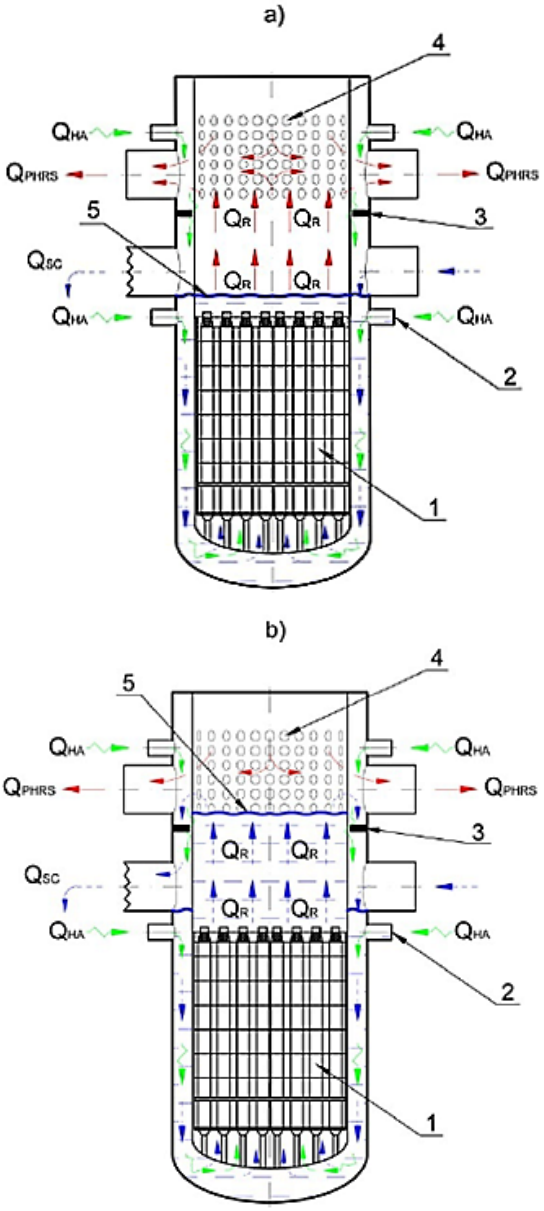

Figure 7: In the case of LOCA, a mass transfer of boric acid takes place in the VVER reactor vessel (Kopytov *et al.,* 2009a); a) First stage of accident; b) Second stage of accident: 1) reactor core; 2) emergency core cooling equipment nozzle; 3) separating collar; 4) reactor barrel perforations; 5) liquid content; coolant flow, steam and condensate boric acid solution intake from the HA systems; QR: denotes the amount of heat energy emitted in the reactor; QSC: the amount of energy released by steam when it passes through a leak and into the containment; The water from hydro accumulators removes energy from the core which is referred to as QHA. QPHRS: heat energy taken from the core as a result of PHRS operation.

Table 1 shows the evolution of latent heat (NRC) in the reactor core since it has been shut down (Kopytov *et al.*, 2009b). The flow rate parameters used for calculations from HA-2 passive hydraulic accumulator tanks are given in table 2 as input data.

Table 1
Residual heat in the VVER core (Schmal & Ivanov,2015)

Time (second)	Residual heat (MW)
100	0.0331
1000	0.0206
10000	0.0105
$28.8 \cdot 10^3$	0.0077
$37.8 \cdot 103$	0.0072
$50 \cdot 10^3$	0.0067
$100 \cdot 103$	0.0055
$130 \cdot 10^3$	0.0053
$500 \cdot 103$	0.003
$147 \cdot 104$	0.0022
$216 \cdot 104$	0.0018

Table 2
Parameters of systems of passive VVER core reservoir of hydraulic accumulation tanks (Schmal & Ivanov, 2015)

Parameter	Value (HA-2)	Value (HA-2)	Value (HA-2)	Value (HA-2)
The stage's duration, s	100 – 5430	5431 – 10860	10861 – 29000	86401 – 259200
Flow rate of boric acid solution, kg/s	10.0	5.0	3.3	1.6

B. Simulation by MATHCAD

Real scenarios of emergency condition like pressure, temperature was simulated in the experimental test facility and then boric acid concentration data was obtained. The data collected from the test facility was used in several equations (for example- steam flow rate, boric acid solution flow rate etc.) in MATHCAD software. The results obtained from subsequent MATHCAD calculations were used to analyze the results of boric acid concentration graphs, flow rates, mass of boric acid etc. at emergency situation.

There is a variety of dependencies that make determining the importance of steam moisture possible. For example, for determining the water content of steam, the formula is:

$$w = 2.75 \times 10^8 \frac{N^{2.3}}{Ga^{1.1}\left[\frac{\rho''}{\rho'-\rho''}\right]^{0.25}} \quad (1)$$

Where $N = w_0''^2/(\varphi g H)$

However, this dependency is only valid for measuring steam water content when the increase in steam is equal to or less than 1 m, which is considerably less than what is observed in case of VVER reactor. Furthermore, there are

dependencies that enables the calculation of steam content of a steam water mixture flow x:

$$x = 0.26\left(\frac{w_0''}{g\sqrt{\sigma/g(\rho'-\rho'')}}\right)^{0.36}\left(\frac{\rho''}{\rho'-\rho''}\right)^{0.12} \quad (2)$$

The findings of experimental tests performed on a large-scale test facility at the SSC RF-IPPE were used to determine the condensation efficiency of steam generators.

$$N_{PHRS} = 144.8 - 5.885\cdot 10^{-4}\tau + 1.499\cdot 10^{-9}\tau^2 - 131.25 + 7.619\cdot\frac{10^4}{\sqrt{\tau}} \quad (3)$$

NPHRS is the steam generator's condensation capacity, kW; t is the time, s

The mass of evaporated water over time will be as follows:

$$\Delta m_s(H_2O) = \frac{N_{RC}}{h''-h_{RPC}}\Delta\tau \quad (4)$$

Mass of the condensate formed in the steam generator due to the operation of PHRS and the mass of boric acid solution introduced into the reactor via the hydro-accumulators are:

$$\Delta m_m(\text{solution}) = (G_{HA} + G_{PHRS})\Delta\tau \quad (5)$$

The following is the mass of boric acid that entered the reactor via HAs:

$$\Delta m_m(H_3BO_3) = G_{HA}C_{HA}(H_3BO_3)\Delta\tau \quad (6)$$

The following is the quantity of boric acid solution which enters the containment:

$$\Delta m_{out}(\text{solution}) = \Delta m_m(\text{solution}) - \Delta m_s(H_2O) \quad (7)$$

As a result, during the first phase of the emergency procedure, the following formula is employed to compute the boric acid concentration in the reactor core:

$$C_i(H_3BO_3) = \frac{(m_{RC}+m_{RPC})C_{i-1}+\Delta m_{in}(H_3BO_3)}{m_{RC}+m_{RPC}+\Delta m_{in}(\text{solution})-\Delta m_s(H_2O)} \quad (8)$$

With time, the quantity of residual heat releases reduces along with the quantity of foamed water in the reactor.

The distance between the bottom generator of the "cold" loop of the main circuit and the top row of perforations hole in the reactor barrel is 1.845 meters and the distance between both the top of the core as well as the upper perforation holes in the core barrel is 2.77 meters. The essential steam content when the foamed water volume increases over the top row of perforations in the barrel, in the emergency situations, with a "cold" leg break is:

$$\varphi_{CR} = \frac{1.845}{2.77} = 0.666$$

The following is the formula for estimating steam content:

$$x = 0.26\left(\frac{w_0''}{g\sqrt{\sigma/g(\rho'-\rho'')}}\right)^{0.36}\left(\frac{\rho''}{\rho'-\rho''}\right)^{0.12} \quad (9)$$

Where, steam velocity:

$$w'' = N_{RC}/r\cdot\rho''\cdot F_{cs} \quad (10)$$

Residual heat energy will heat up the boric acid solution and that will infiltrate the core from the RPC and evaporate later, in the second stage of the accident:

$$N_{RC} = G_N r + G_{12}(r + h' - h_{RPC}) \quad (11)$$

Because of droplet entrainment mechanisms, the boric acid flow rate exiting both RPC and the core has increased G_{Re} as $G_{Re} = \omega G_m$.

The steam-water combination departing the reactor which comprises of boric acid droplets and steam is substituted with boric acid solution via the RPC:

$$G_{12} = G_N + G_{Re} \quad (12)$$

The following expression shows how mass of boric acid varies in the core over time:

$$\Delta m_{RC}(H_3BO_3) = (G_{12}C_{RPC} - G_{Re}C_{RC})\Delta\tau \quad (13)$$

As previously said, the boric acid solution through reactor pressure chamber would flow through the core at a flow rate of G12, with the excess solution being drained into the containment via the ruptured main circulation pump. The mass of the spilled solution in the containment over duration as well as the variation in mass of boric acid in the quantity of reactor pressure chamber (RPC) over the same time span may be calculated using this method:

$$G_{SC} = G_{HA} + G_{PHRS} + G_{Re} - G_N \quad (14)$$

$$\Delta m_{RPC}(H_3BO_3) = (G_{HA}C_{HA} + G_{Re}C_{RC} - G_{12}C_{RPC} - G_{SC}C_{RPC})\Delta\tau \quad (15)$$

To calculate the remaining heat, we use the following formula to compute the evaporation rate:

$$N_{RC} = G_N[(h'' - h_{RPC}) + \omega(h' - h_{RPC}) \quad (16)$$

As a result, the steam flow rate is as follows:

$$G_N = N_{RC}/(h'' - h_{RPC}) + \omega(h' - h_{RPC}) \quad (17)$$

The following expression shows the change in boric acid content in reactor core throughout time:

$$\Delta C_{RC}((H_3BO_3) = \Delta m_{RC}\left(\frac{(H_3BO_3)}{m_{RC}}\right) \quad (18)$$

4. RESULTS AND DISCUSSION

Changes in concentration of boric acid in the reactor core and reactor pressure chamber are calculated using the equations and assumptions listed above. The concentration of boric acid in the tanks of the passive core re-flooding systems is currently $16\,g/kg$ H2O according to NPP operating legislation (Kalyakin *et al.*, 2003). Variants of decreasing H_3BO_3 concentration in $HA-2$ method to $16g/kg\ H_2O$ are included in this measurement. From the experiment, we got the data of boric acid concentration at specific parameters – for example, at a specific pressure and temperature. Then this data obtained from the experiment has been used in calculations to analyse how the boric acid concentration changes over time and helps us to investigate whether the boric acid reaches the point of crystallization within 24 hours of a large loss of coolant accident. So, the experiment gives us the starting/input data that is used for numerical analysis in MATHCAD. So, the primary data is given by the experiment and the final result comes from the numerical analysis.

Figure 8(a) and 8(b) shows the results of the numerical analysis. Figure 8(a) shows the concentration curve of

boric acid in the event of boric acid (H_3BO_3) solubility with steam and 8(b) indicates the concentration curve of boric acid in the event of boric acid (H_3BO_3) solubility without steam. The amount of boric acid that accumulates in the reactor core after an emergency process can be seen. It is important to note that the boric acid concentration in the reactor core is $0.311\,kg/kg$ after 24 hours of emergency phase and does not exceed the solubility maximum. The solubility limit (C Limit) is about $0.415\,kg/kg$ at water saturation temperature. The value of boric acid drop entrainment from the core was assumed to be 0.2 percent during this measurement. Figure 8(a) was calculated using the normal value for steam moisture at the steam generator's output. $\tau_{\varphi.cr}$, the green line divides the emergency period during accident. In Figure 8(a), the blue line indicates the boric acid concentration in the accidental period. We found that at the primary stage of emergency process, the boric acid concentration is more or less constant.

After the first stage of hydro accumulators operate, second stage hydro accumulators start to operate and we see that during the time period of second stage hydro accumulator operation, the concentration of boric acid gradually increase. From numerical analysis in MathCAD, it is found that the final concentration of boric acid with the steam solubility is about $0.153\,kg/kg$. But it is much below the limiting boric acid concentration (C Limit). And the yellow line indicates the limiting concentration ($0.415\,kg/kg$) of boric acid.

So, in Figure 8(b) we see that boric acid concentration curve is almost similar with the previous result. This graph indicates the boric acid concentration (brown line) without steam solubility in accordance with time range of whole emergency process. As we can see in Figure 8(b), the boric acid's concentration of core is more or less constant during the initial stage of emergency process. Then with the operation of hydro accumulator second stage the boric acid's concentration curve goes slightly higher. By calculation, we found that after 24 hours of operation of hydro accumulator second stage, the concentration amount (without solubility of steam) is found $0.158\,kg/kg$. But most importantly, it is also significantly below the limiting concentration of boric acid (blue line).

The concentration of boric acid in reactor pressure chamber (RPC) was fluctuating a little bit during initial emergency process and after the second stage hydro accumulator operation, the concentration graph of boric acid decreases sharply and become constant. Because there is a flow rate of condensate from steam generator with zero boric acid solution and it is mixing with boric acid solution from the HA-2 system, so, the final concentration is low. And another reason is that, there is no boiling condition in RPC, the concentration of boric acid has not increased like in the core. But importantly, it is also substantially lower than the boric acid limiting concentration. (blue line). So, for VVER-1200, the hydro-accumulator 2nd stage operation during an emergency process prevents the accumulation of boric acid in the core as well as in the reactor pressure chamber (RPC). These states are proved by this calculation.

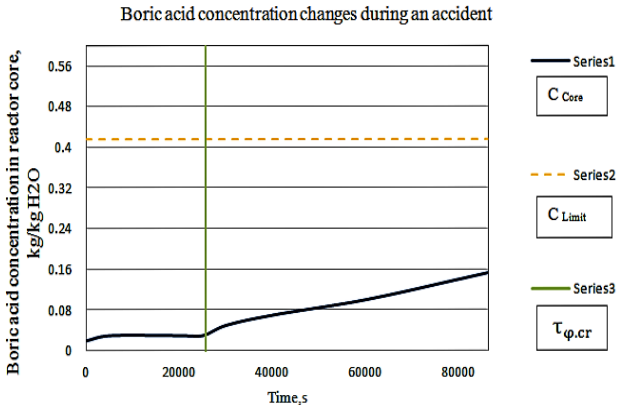

(a)

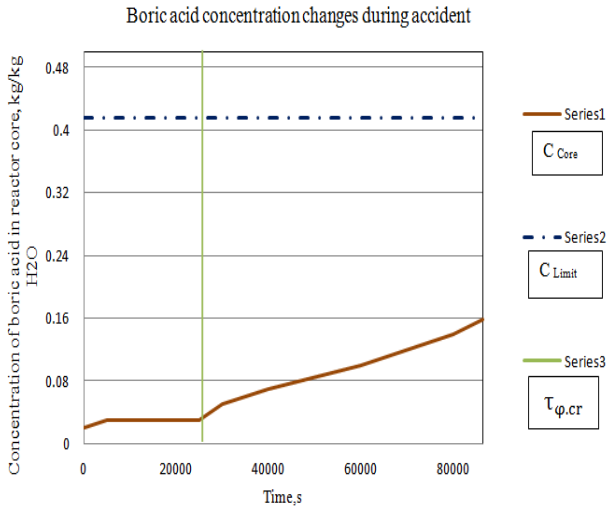

(b)

Figure 8: (a) The concentration of boric acid in the reactor core changes (with solubility of steam), (b) The concentration of boric acid in the reactor core changes (without solubility of steam)

As previously said, deposits of boric acid in the core have a direct effect on heat recovery during the emergency procedure. So, the mass of the boric acid deposit was calculated as well. The following formula was used to quantify the deposit mass, $m_{dep}(H_3BO_3)$:

$$m_{dep}(H_3BO_3) = m_{RC}(C_{RC}(H_3BO_3) - C_{lim} \quad (19)$$

During the measurement analysis, it was discovered that the available dependencies for estimating steam moisture and steam quality of the medium at the VVER core's outlet in the event of an emergency are currently unknown. These variables are critical for understanding boric acid mass transport processes. Experiments on the mass transfer processes of H3BO3 should be carried out at parameters that are equivalent to the emergency mode parameters of VVER reactors to remove current uncertainties. By calculation analysis it is seemed that flow rates of hydro-accumulators and PHRS (passive heat removal systems) decreases with the period of time. The HA-2 flow rates are given in Table 2 previously. The flow rate of HA-2 decrease at a constant rate and it is very effective to cool down the reactor core and reactor pressure chamber as

well. And the passive cooling through steam generator (PHRS) flow rate is also decrease with the period of time as shown in Figure 9.

We see that the GPHRS is decreasing in the graph continuously because of low steam production in the reactor core with the time. The flow rate of PHRS becomes 8.2 kg/s after whole emergency process and it prevents the crystallization of boric acid in the reactor core and containment volume (CV). So, these following graphs describe enough to study the flow rates of hydro-accumulators 2nd stage and passive heat removal systems through steam generators. Figure 6 shows the change of flow rates of PHRS and hydro-accumulator 2nd stage in the core throughout the entire emergency situation. During calculations it is seemed that there is no precipitation of boric acid occurs. So, $mprecipitation = 0$ during 24 hours after an accident so there is no precipitation line in the following Figure. So, the deposit mass of boric acid in the reactor core is almost zero after initial emergency process. The blue line indicates the flow rate of $HA-2$ which gradually decreases stage by stage. In the final stage the flow rate is become constant which is 1.6 kg/s.

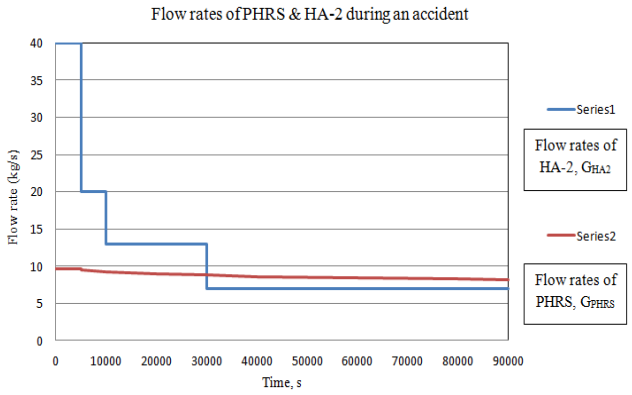

Figure 9: Change of flow rates of PHRS and hydro-accumulator 2nd during the whole emergency process

In Figure 10, the flow rate of boric acid due to droplet entrainment is observed (green line), after being critical the flow rate is decreasing according to the time. In the initial stage of emergency process, the values of droplet entrainment are impossible to be measured because the water level is too low inside the core.

And boric acid flow rate from RPC to core is constant (red line) during the emergency process. During calculation, it is found that a significant amount of boric acid escapes from reactor core as well as containment volume with steam and droplet entrainment process. Because, we know that during emergency, reactor core is in boiling state, so, when boric acid solution enters into the core, maximum solution turns into vapor which contains boric acid. Then the steam with boric acid comes out from reactor core to containment volume. As we know that droplet entrainment is an entrapment of substances, so with liquid, boric acid is entrapped and comes out through the rupture of main circulation pipelines. It is very helpful to prevent the boric acid accumulation or deposit mass of boric acid inside the core and containment volume during the whole emergency process. After 24 hours of initial emergency conditions it is found that no precipitation of boric acid is found inside area or active area of the reactor.

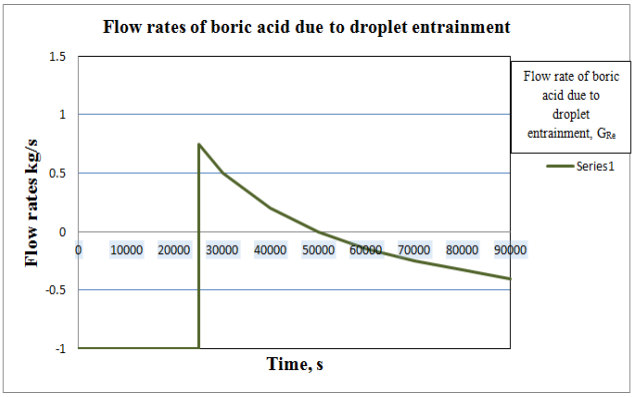

Figure 10: Change of boric acid flow rate in the core because of droplet entrainment during the whole emergency process

5. CONCLUSION

The determination of boric acid mass transfer processes plays a significantly role in the analysis of emergency mode operations in modern VVER reactors. In the VVER-1200 reactor core, the computed estimation revealed a considerable amount of concentration of boric acid 24 hours after the incident began. This process may not result in crystallization on the surface of the fuel rods and do not hamper in heat removal through the core. It should be noted that the estimation was based on a set of conservative values that did not take into consideration the removal of solution of boric acid from the core due to the capacity of steam to dissolve it. During the calculation study, it was discovered that the available dependencies for estimating steam moisture as well as steam content of the mediums at the VVER core's exit in the event of an emergency are currently questionable. Because, at such emergency situation, the steam moisture and steam content parameters vary which leads to an uncertainty in variable dependencies. These variables are critical for understanding the boric acid mass transfer mechanisms. Experiments on the mass transfer processes of H3BO3 should be carried out at parameters that are equivalent to the emergency mode parameters of VVER reactors to remove current uncertainties.

NOMENCLATURES

G	Factor of gravity
σ	Liquid tension
h''	Steam enthalpy at saturation temperature (kJ/kg)
h_{RPC}	Boric acid solution enthalpy in RPC (kJ/kg)
G_{HA}	Boric acid solution flow rate from HA (kg/s)
G_{PHRS}	The flow rate of condensate in SG (kg/s)
m_{RC}	Mass of boric acid solution in core (kg)
m_{RPC}	The amount of boric acid solution in RPC (kg)
G_N	Steam output rate (kg/s)
G_{12}	Rate of flow of a boric acid solution to the core via RPC (kg/s)
r	Evaporation specific heat (kJ/kg)

h' The enthalpy of water is at saturation temperature (kJ/kg)
h_{RPC} Boric acid solution enthalpy in RPC (kJ/kg)
C_{RPC} Boric acid solution concentration in RPC (kg/kg)
C_{RC} In the core of the reactor, the concentration of boric acid solution (kg/kg)
G_m Flow rate of steam-water combination (kg/s)

RECOMMENDATIONS

Unfortunately, this work was limited to the calculation in the time range of 24 hours of emergency condition. It would be great to do the application of this calculation methodology as well as the results obtained for the case with operation of VVER third-stage hydraulic accumulators (up to 72 hours).

ACKNOWLEDGEMENTS

This work was supported by the Department of Nuclear Physics and Engineering, National Research Nuclear University (MEPhI), Moscow, Russia.

REFERENCES

Cohen, P. (1973). Water technology of power reactors. Springer Publishing.

Hassan, A. Y., Osturk, S., & Lee, S. (2015). Progress in Nuclear Engineering. Progress in Nuclear Engineering, 85, 239–253.

Hewitt, G. F., & Hall-Taylor, N. S. (1970). Annular Two-phase Flow (136–148). Pergamon Press, N. Y.

Ishii, M., & Grolmes, M. A. (1975). AIChE Journal. Inception Criteria for Droplet Entrainment in Two-Phase Concurrent Film Flow, 21(2), 308–318.

Kalyakin, S. G., Remizov, O. V., Morozov, A. V., YU.S., Y. U. R'. E. V., & YU.V., K. L. I. M. A. N. O. V. A. (2003). Proceedings of Graduate Schools. Nuclear Power Engineering. Substantiation of Design Functions of the Passive Flood System HA-2 for Improved NPP Project with VVER Reactor, 2, 94–101.

Kalyakin, S. G., Sorokin, A. P., Pivovarov, V. A., Pomet'ko, R. S., Selivanov, Y. U. F., Morozov, A. V., & Remizov, O. V. (2014a). Atomic energy. Experimental Studies of the Thermo Physical Processes in Justification of the Safety of the New Generation of VVER, 114(4), 241–246.

Kalyakin, S. G., Sorokin, A. P., Pivovarov, V. A., Pomet'ko, R. S., Selivanov, Y. U., Morozov, A. V., & Remizov, O. V. (2014b). Atomnaya energiya. Experimental Research of Thermal Physical Processes for the Safety Substantiation of New Generation VVER, 116(4), 241–246.

Kopytov, I. I., Kalyakin, S. G., Berkovich, V. M., Morozov, A. V., & Remizov, O. V. (2009a). Experimental investigation of non-condensable gases effect on Novovoronezh NPP-2 steam generator condensation power under the condition of passive safety systems operation. Proceedings of theXYII-th International Conference on Nuclear Engineering, ICONE17. International Conference on Nuclear Engineering, ICONE17, Brussels.

Kopytov, I. I., Kalyakin, S. G., Berkovich, V. M., Morozov, A. V., & Remizov, O. V. (2009b). Proc. 17 Int.Conf. on Nuclear Engineering. 735–743.

Morozov, A., & Sakhipgareev, A. (2017). Experimental estimation of the effect of contact condensation of steam–gas mixture on VVER passive safety systems operation. Nuclear Energy and Technology, 3(2), 98–104. https://doi.org/10.1016/j.nucet.2017.05.002

Morozov, A. V., & Remizov, O. V. (2012a). Teploenergetika. Experimental Justification for Design Functions of Additional Passive Re Flooding Systems of the Reactor VVER Core., 5, 22–27.

Morozov, A. V., & Remizov, O. V. (2012b). Thermal Engineering. Experimental Substantiation of Design Functions of the VVER Auxiliary System of Passive Core Reflooding, 5, 22–27.

Morozov, A. V., & Remizov, O. V. (2012c). Thermal Engineering. Experimental Study of VVER Steam Generator Model Operation in Condensation Mode, 5, 16–21.

Morozov, A. V., & Remizov, O. V. (2012d). Thermal Eng: Vol. 59 (365–370). Springer Publishing. https://doi.org/10.1134/S0040601517050044

Morozov, A. V., Remizov, O. V., & Tsyganok, A. A. (2009). Proceedings of Graduate Schools. Nuclear Power Engineering. Experimental Study of Non-Equilibrium Thermal-Hydraulic Processes in a Passive VVER Core Reflooding System, 4, 115–123.

Newitt, D. M., Dombrowski, N., & Knelman, F. H. (1954). Trans. Inst. Chem. Eng. "Liquid Entrainment: I, The Mechanism of Drop Formation from Gas or Vapor Bubbles, ", 32, 244.

Schmal, I. I., & Ivanov, M. A. (2015a). Boric acid mass transfer processes in accidental conditions. Proc. of the 9th Int. Scientific and Technical Conference «Safety Assurance of VVER NPP». Podolsk, JSC EDO «Gidropress». Published.

Schmal, I. I., & Ivanov, M. A. (2015b). Boric acid mass transfer processes in accidental conditions. 25–29.

Schmal, I. I., & Ivanov, M. A. (2015c). Safety assurance of NPPs with WWER. 25–29.

Vallée, C., Höhne, T., & S. (2008). Two-phase flow phenomena, Experimental Investigation and CFD Simulation of Horizontal Stratified Two-Phase Flow Phenomena, 238(3), 637–646.

MIJST
MIST International Journal of Science and Tenchnology

Predicting Fully-developed Channel Flow with Zero-equation Model

M. M. Rahman[1*], K. Hasan[2], Wenchang Liu[3], and Xinming Li[4]

Hangzhou Dianzi University, School of Mechanical Engineering, 310018 Hangzhou, China

emails: *[*1]mizanur_rahman@hdu.edu.cn; [2]m.khasan1100@gmail.com; [3]chang910521@foxmail.com; [4]631947731@qq.com*

ARTICLE INFO

Article History:

Received: 28th September 2021
Revised: 16th November 2021
Accepted: 18th November 2021
Published: 23rd December 2021

Keywords:

y-phrases
Algebraic model
SED theory
Stress length
Stress-intensity parameter
Wall turbulence

ABSTRACT

A new zero-equation model (ZEM) is devised with an eddy-viscosity formulation using a stress length variable which the structural ensemble dynamics (SED) theory predicts. The ZEM is distinguished by obvious physical parameters, quantifying the underlying flow domain with a universal multi-layer structure. The SED theory is also utilized to formulate an anisotropic Bradshaw stress-intensity factor, parameterized with an eddy-to-laminar viscosity ratio. Bradshaw's structure-function is employed to evaluate the kinetic energy of turbulence k and turbulent dissipation rate $\boldsymbol{\varepsilon}$. The proposed ZEM is intrinsically plausible, having a significant impact on the prediction of wall-bounded turbulence.

NOMENCLATURE

C_μ	eddy-viscosity coefficient
DNS	Direct Numerical Simulation
k	turbulent kinetic energy
l_{12}	stress length
R_T	eddy-to-laminar viscosity ratio
S	mean strain-rate
SED	Structural ensemble dynamics
SST	shear stress transport
u_i	Cartesian velocity components
u_T	friction velocity
Y	wall distance
y^+	$u_\tau y/\nu$
ZEM	zero-equation model
γ	compensated stress length
p	pressure
R_b	stress-intensity factor
Re	Reynolds number
ε	turbulent dissipation rate
θ	momentum thickness
κ	von-Karman constant
μ, μ_T	laminar & turbulent eddy viscosities
ν	laminar kinematic viscosity
ρ	density
ω	specific dissipation rate Subscript
i, j	variable quantities
T	turbulent condition

1. INTRODUCTION

Due to the lack of a relevant existing theory which concentrates on the physical understanding of wall turbulence, the framework of the RANS (Reynolds-averaged Navier-Stokes) turbulence model takes a pivotal role (Durbin, 2018) on this deficiency. The formulation of turbulence model typically becomes complicated when introducing correlation artefacts to predict a new flow with original features; correlation terms having dimensional argument retain several functions or coefficients without physical interpretations. In principle, the concept of wall turbulence with its universal structure can avoid a large

amount of empiricism involved in wall-bounded flows. Unfortunately, the Prandtl mixing length theory (Prandtl, 1925), von Karman log-law argument (Segalini *et al.*, 2013) and Townsend similarity hypothesis (Townsend, 1976) are not fully capable of providing a consistent route to the development of a zero-equation model (ZEM). The current research convokes such an alternative to developing a plausible algebraic model, resorting to a well-established wall-turbulence phenomenon.

Using a symmetry-based approach, the SED (structural ensemble dynamics) theory (She *et al.*, 2009, 2010, 2017) has been recently proposed. The concept applies an invariant wall restriction on turbulence eddies in the framework of a generalized Lie-group dilation invariance (LDI) to the stress length l_{12}, estimating scales of eddies. The SED theory speculates a multi-layer formulation for l_{12} with a fully-developed channel flow. The analytic solution preserves the information of the entire flow domain with a four-layer structure; four layers consist of a viscous sublayer, buffer layer, bulk flow region (containing log-layer) and core layer. The four-layer structure precisely characterizes the total flow field and captures the genuine similarity image of wall turbulence with an increase in Reynolds number. The SED theory is capable of predicting its universal analytic etiquette sticking to an LDI principle, which is apparently universal in the presence of a wall. Remarkably, the variations in multi-layer parameters represent disparities among various layers of a physical flow domain.

A zero-equation (an algebraic) turbulence model is developed in the current study, adhering to the impressive multi-layer physics of wall turbulence. The turbulent kinematic eddy viscosity is calculated as $\nu_T = l_{12}^2 S$, where S is the strain-rate invariant. Bradshaw's stress-intensity factor [8] is formulated using the SED theory which is parameterized with an eddy-to-laminar viscosity ratio; the resulting structure-function can reasonably predict the kinetic energy of turbulence k and turbulent dissipation rate ε. Predictions from the widely-used SST (shear-stress-transport) *k-ω* turbulence model [9] are compared with those of the ZEM. Results demonstrate that the ZEM performs better than the SST model. A remarkable achievement can be ascribed to the current work in a way that the wall turbulence with a refined physical multi-layer description has prevailed over the drawbacks of previously developed algebraic turbulence models (Prandtl, 1925; Segalini *et al.*, 2013; Townsend, 1976; Wilcox, 2006).

2. GOVERNING EQUATIONS

The stress length of SED theory has specified the turbulent eddy-viscosity in the new algebraic model. The current model begins from RANS equations which deal with the mean conservation of mass and momentum. RANS equations can be represented as follows:

$$\frac{\partial \rho}{\partial t} + \frac{\partial}{\partial x_i}\left(\rho u_i\right) = 0 \tag{1}$$

$$\frac{\rho u_i}{\partial t} + \frac{\partial}{\partial x_j}\left(\rho u_i u_j\right) = -\frac{\partial p}{\partial x_i} + \frac{\partial \sigma_{ij}}{\partial x_j} \tag{2}$$

where u_j is the *jth* component of velocity, x_j represents Cartesian coordinates, ρ implies the fluid density and p denotes the pressure. The Boussinesq approximation can be applied to relate total stresses σ_{ij} with the mean strain-rate tensor S_{ij} as:

$$\sigma_{ij} = 2\left(\mu + \mu_T\right)\left(S_{ij} - \frac{1}{3}S_{kk}\delta_{ij}\right), S_{ij} = \frac{1}{2}\left(\frac{\partial u_i}{\partial x_j} + \frac{\partial u_j}{\partial x_i}\right) \tag{3}$$

where the Kronecker's delta functionis indicated by δ_{ij}; δ_{ij} = 1 for $i = j$ and δ_{ij} = 0 for $i \neq j$. Laminar and turbulent viscosities are designated by μ and μ_T, respectively. According to the SED theory, μ_T can be defined using the stress length function l_{12} as:

$$\mu_T = \rho l_{12}^2 S$$

where the mean strain-rate invariant S is given by $S = \sqrt{2S_{ij}S_{ij}}$. A sub-concept of the SED theory, regarded as the order-function formula of She *et al.* (2010) describes complex systems with multi-layer structures; the wall turbulence belongs to this group. According to the SED theory, a well-defined set of functions in the framework of multi-products (i.e., order functions) is used to format the multi-layer structures. The order function is deduced from a quantitative analysis of the generalized LDI, established with the presence of wall. The order-function generic form can be given as:

$$\phi = c_0\left(\frac{y}{a_0}\right)^{c_0/b_0}\prod_{i=1}^{n}\left[1+\left(\frac{y}{a_i}\right)^{b_i}\right]^{c_i/b_i} \tag{5}$$

where a, b and c can be adjustable constants; φ is an order function having complex multi-layer structures, parameterized with a variable y and n is the number of products. In fact, the spatial variation of φ involves multiple transitions, from one layer to another. Some soft-wares like MATLAB or Mathematica can assist the curve-fitting process. The SED hypothesis speculates that in the fully-developed turbulent boundary layer, a multi-layer form is associated with the stress length l_{12}. It provides (She, 2017):

$$l_{12}^+ = l_0\left(\frac{y^+}{9.7}\right)^{3/2}\left[1+\left(\frac{y^+}{9.7}\right)^4\right]^{1/8}\left[1+\left(\frac{y^+}{41}\right)^4\right]^{-1/4} \frac{1-r^4}{4(1-r)}\left[1+\left(\frac{0.27}{r}\right)^2\right]^{1/4} \tag{6}$$

where $y^+ = yu_\tau/\nu$ is the dimensionless wall-distance with the friction wall-velocity $u_\tau = \sqrt{(\nu S)_w}$ which is well-defined for attached and mild separated flows with $S_w > 0$; the kinematic laminar viscosity is given by $\nu = \mu/\rho$. In addition, $r = 1 - y/\delta = 1 - y^+/\mathrm{Re}_\tau$, where δ is the channel half-width and $\mathrm{Re}_\tau = \delta u_\tau/\nu$ signifies friction Reynolds number. Equation (6) retains a canonical four-layer structure of wall turbulence, consisting of a viscous sublayer, buffer layer, bulk zone and core layer for a fully-developed channel flow. They remain apart from each other by empirically evaluated layer thicknesses, respectively $y^+_{sub} = 9.7, y^+_{buf} = 41$ and $r_{core} = 0.27$. In other words, the viscous sublayer ending at $y^+_{sub} = 9.7$ is the first layer adjacent to the wall; afterward, the buffer layer ends at $y^+_{buf} = 41$.

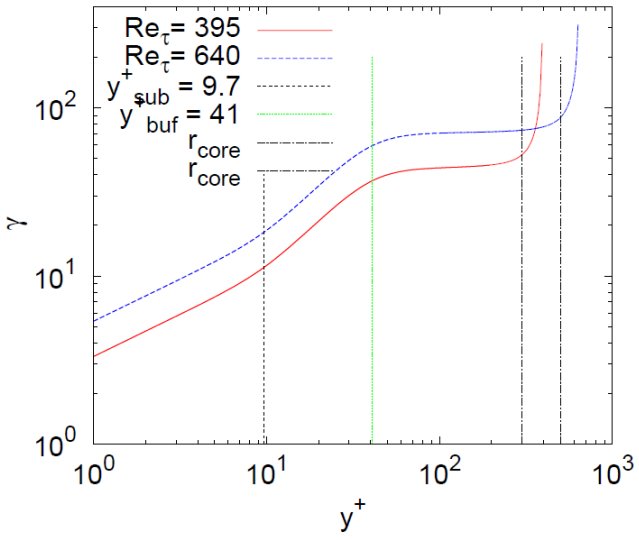

Figure 1: Compensated plot of $\gamma = l^+_{12}/(1-r^4)$. The bulk layer (between y^+_{buf} and r_{core}) retains almost constant values. Dashed lines show thicknesses of viscous sublayer $(y^+_{sub} = 9.7)$, buffer layer $(y^+_{buf} = 41)$ and core layer $(r_{core} = 0.27)$

The core layer expands from the centre-line to a core layer thickness of $r_{core} = 0.27$ and the bulk-flow region consists of the remaining flow domain. In principle, the need for defining overlap region is avoided by the structure of geometry-dependent bulk-flow, i.e., (1 − r^4). It is not difficult to verify that for y$^+$ > 41, the celebrated linear law $l^+_{12} \approx ky^+$ is obtained as a matching function between inner and outer regions with $l_0 \approx 9.7^2\kappa/41 \approx 1.0$, where the Karman constant $\kappa = 0.45$ has been chosen from the original SED theory.

Near the centre $r \le r_{core}$ (with r = 1 − y/δ is the distance from the channel centre-line), a core layer has been defined wherein dissipation and pressure-strain are balanced by turbulent transport that takes over production (She, 2017). In principle, such shifts in the balancing mechanism induce the four-layer structure as mentioned earlier. The multi-layer structure can also be observed in the compensated plot (divided by 1−r^4), as displayed in Figure 1; core layers are at y^+_{core} = (300; 500) for Re_τ = (395; 640). Direct Numerical Simulation (DNS) data are available from (Mansour *et al.*, 1988; Kawamura *et al.*, 1999).

The current study deals with the zero-equation model (ZEM). However, turbulence quantities can be evaluated from turbulence fluctuations using unsteady RANS computations.

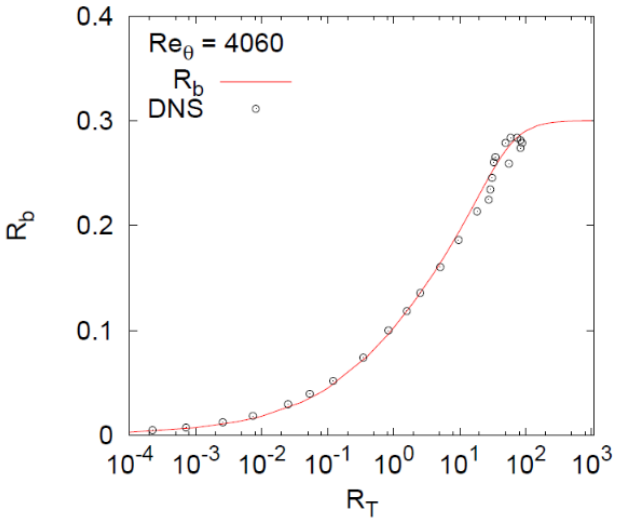

Figure 2: Stress-intensity parameter for flat-plate boundary layer flow at Re_θ = 4060

An extension of the Bradshaw hypothesis (Bradshaw *et al.*, 1967) from free shear flows to wall-bounded flows convokes a plausible parameter, resolving near-wall anisotropy of turbulence. The Bradshaw parameter $R_b = |-uv|/k \approx \sqrt{C_\mu}$, where $|-uv|$ is the principal shear stress, k implies the kinetic energy of turbulence and C_μ = 0.09. It is also believed that the SED theory is precisely accurate to formulate a variable Bradshaw structure-function R_b in the vicinity of the boundary layer. In Reference [12], R_b is fabricated as a function of $R_T = \sqrt{k}\,y/\nu$. Nevertheless, the present formulation necessitates R_b as a function of $R_T = \nu_T/\nu$ (eddy-to-laminar viscosity ratio, where $\nu_T = \mu_T/\rho$ is the kinematic eddy-viscosity) to empirically evaluate k and dissipation-rate ε . Applying the curve-fitting approximation (Equation (5)), the structure parameter R_b is obtained after the calibration with DNS data for a fully-developed turbulent flat-plate boundary-layer flow (Schlatter & Orlu, 2010):

$$R_b = \frac{C_1 R_T^{0.4}}{(1.0 + R_T)^{0.16}\left(1.0 + C_2^2 R_T^2\right)^{0.12}} \qquad (7)$$

where $C_1 = C_\mu^{0.9}$, $C_2 = C_\mu / 5.0$. As $R_T \to \infty$, $R_b \approx C_1 / C_2^{0.24} \approx \sqrt{C_\mu}$. The present work has three products with n = 2. As can be observed from Figure 2, Eq. (7) has a good correspondence with DNS data (Schlatter & Orlu, 2010) of a fully-developed turbulent flat-plate boundary layer at a slice of Re_θ = 4060 (with wake-layer DNS data mostly excluded), where Re_θ signifies the momentum-thickness Reynolds number. The dimensionless turbulent viscosity is calculated as $v_T^+ = \left|-uv^+\right| / \left(du^+/dy^+\right)$ using the DNS data. The structure parameter $R_b = v_T \tilde{S} / k$ can be employed to calculate k and ε as:

$$k = \frac{v_T \tilde{S}}{R_b + C}, \quad \varepsilon = R_b k \tilde{S} \tag{8}$$

where C = 0.01 is used to avoid the near-wall singularity and ε vanishes at the solid wall. It is worth mentioning that on a channel-flow centre-line or outside a boundary layer, the strain-rate invariant S may approach zero. Therefore, the free-stream strain-rate correction S_α with a non-vanishing identity can be convoked as a remedy; it can be approximated from a nearly homogeneous shear flow of Champagne *et al.* (1970) as presented in Equation (9) where the added S_α has a tiny numerical effect.

$$\tilde{S} = \sqrt{S^2 + S_\alpha^2}, \quad S_\alpha = \frac{1}{C_\mu} s^{-1} \tag{9}$$

3. COMPUTATIONS OF FULLY-DEVELOPED TURBULENT CHANNEL FLOW

Fully-developed turbulent channel flows at Re_τ = (395; 640) are simulated to assess the model competency in reproducing near-wall turbulence. Computations are carried out in the half-width of a channel, employing a 1-D (one-dimensional) RANS solver. A non-uniform 1 × 64 grid resolution for Re_τ = 395 and 1×128 grid resolution for Re_τ = 640 are presumably adequate to accurately predict characteristics of the flow (e.g., producing almost grid-independent solutions). To assure the viscous sublayer resolution, the first near-wall cell height is located at $y^+ \approx$ 0.3 to assure the viscous sublayer resolution. A cell-centred finite-volume approach is utilized along with SIMPLE algorithm. Predictions of the present zero-equation model (ZEM) are compared with the well-known Menter SST (shear-stress-transport) model (Menter, 1994).

For a 1-D incompressible flow, the streamwise (x-direction) mean momentum equation can be given as:

$$\frac{\partial p}{\partial x} + \frac{\partial}{\partial y}\left[\left(v + v_T\right)\frac{\partial u}{\partial y}\right] = 0 \tag{10}$$

where the positions of lower and upper walls of the channel are indicated by *y = (−h; h)*. Since the mean flow field has a 1-D identity, the axial gradient of pressure $\partial p / \partial x$ remains constant, and the continuity constraint $\partial u_i / \partial x_i$ = 0 is naturally satisfied. However, $\partial p / \partial x$ must be computed as a part of the solution method since the pressure gradient is not known a priori. The pressure-velocity correction method (Rahman *et al.*, 1996, 1997) is an appropriate choice to solve the problem. The scheme continually updates the velocity and axial pressure gradient as long as the mass imbalance is minimized.

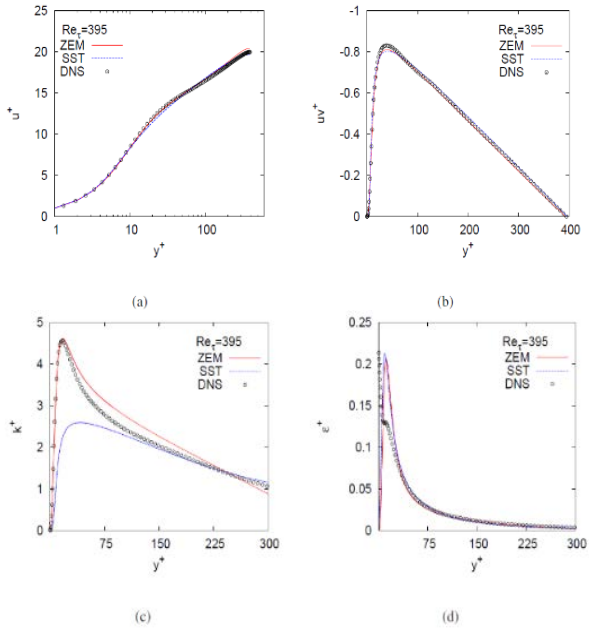

Figure 3: Developed channel flow at Re_T = 395: (a) mean velocity; (b) Reynolds shear stress; (c) kinetic energy of turbulence and (d) turbulent dissipation-rate

Simulations from the ZEM and Menter's SST model in wall units are presented in Figures 3 and 4. Comparisons are prepared by plotting results in terms of $u^+ = u/u_\tau$, $uv^+ = uv/u_\tau^2$, $k^+ = k/u_\tau^2$ and $\varepsilon^+ = v\varepsilon/u_\tau^4$ versus y^+. The Boussinesq approximation has been used to calculate the Reynolds shear stress. Figures 3(a) and 4(a) show velocity profiles from independent turbulence models. Simulations of the ZEM and SST model make good correspondence with DNS data. Noteworthily, acceptable congruence of the ZEM with DNS data can be observed without having transport and diffusion effects of the kinetic energy of turbulence and turbulent dissipation rate. Nonetheless, the SST model under-predicts the mean velocity profile in the wake-deficit region of boundary layer at Re_τ = 640. Perceptively, the SST k-ω model inherits this complication. Profiles of Reynolds shear stresses are plotted in Figures 3(b) and 4(b). As can be noticed, predictions of the ZEM and SST model agree well with DNS data; the difference between them is almost indistinguishable.

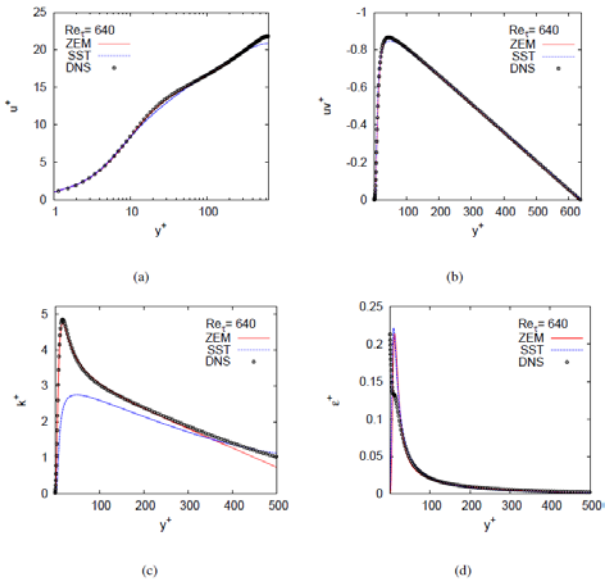

Figure 4: Developed channel flow at Re_T = 640: (a) mean velocity; (b) Reynolds shear stress; (c) kinetic energy of turbulence and (d) turbulent dissipation-rate

Model performances are assessed further with the k^+ profiles, shown in Figures 3(c) and 4(c). As can be observed, the ZEM matches with the DNS data in the near-wall region, whereas the k^+ profiles near the wall are badly under-predicted by the SST model. Figures 3(d) and 4(d) exhibit the ε^+ -profile from the ZEM and SST computations. It is well-known that experimental and DNS data exhibit a maximum ε^+ close to the wall. None of the turbulence models is capable of capturing a maximum ε^+ in the wall-vicinity; however, ε^+ profiles are predicted qualitatively well by both models after the wall regime. In fact, the numerical stability can be strengthened with such a behaviour of the ε^+ -profile in near-wall regions. The SST model experiences an enhancement in the convergence of numerical solvers due to this phenomenon.

4. CONCLUSIONS

Predicted results demonstrate that the ZEM has consistently outperformed the well-known SST model. The success of computation is facilitated by the essence of wall turbulence, comprising a universal multi-layer quantification of the stress length l_{12} which interprets the invariant (wall-normal distribution) of turbulent eddy-viscosity. The formulation of ZEM offers a positive perspective for the RANS model wherein an accurate prediction of wall-bounded flows is enhanced in collaboration with the fundamental understanding of wall turbulence. The ZEM presumably deserves the following specific merits: (a) may produce an accurate constraint on unsteady computations such as detached-eddy or large-eddy simulations; (b) may provide a calibration tool for experimental flow conditions and (c) flows over new geometries with available experimental data, the ZEM may be used to determine corresponding multi-layer parameters (like l_0^+ and y_{buf}^+) which specify the relevant flow physics of turbulent boundary-layer.

DISCLOSURE STATEMENT

No potential conflict of interest is reported by the authors.

ACKNOWLEDGMENTS

We are grateful to Hangzhou Dianzi University research and laboratory establishment supporting funds (Grant Nos. GK208800299001-006 & GK208803299001-013) of Zhejiang Province, P.R. China.

REFERENCES

Bradshaw P, Ferriss DH, Atwell NP: Calculation of boundary layer development using the turbulent energy equations. Journal of Fluid Mechanics, 23:3164;1967. DOI: 10.1017/S0022112067002319

Champagne FH, Harris VG, Corrsin S: “Experiments on nearly homogeneous turbulent shear flow.” Journal of Fluid Mechanics, 41:81139; 1970. DOI: 10.1017/S0022112070000538

Durbin PA: Some recent developments in turbulence closure modeling. Annual Review of Fluid Mechanics, 50:77-103; 2018. DOI: 10.1146/annurev-fluid-122316-045020

Kawamura H, Abe H, Matsuo Y: DNS of turbulent heat transfer in channel flow with respect to Reynolds and Prandtl number effect. International Journal of Heat and Fluid Flow, 20(3):196-207;1999. doi:10.1016/S0142-727X (99)00014-4. DOI: 10.1016/S0142-727X(99)00014-4

Menter FR: Two-equation eddy-viscosity turbulence models for engineering applications. AIAA Journal, 32(8):1598-1605; 1994. DOI: https://doi.org/10.2514/3.12149

Mansour NN, Kim J, Moin P: Reynolds-stress and dissipation-rate budgets in a turbulent channel flow. Journal of Fluid Mechanics, 194:15-44;1988. DOI: 10.1017/S0022112088002885

Prandtl L: Bericht uber Untersuchungen zur ausgebildeten Turbu- lenz. Zeitschrift fur angew. Math. u. Mechanik. 5:136-139; 1925. (in German) DOI: 10.1007/978-3-662-11836-8_57

Rahman MM, Keskinen K, Vuorinen V, Larmi M, Siikonen T: Consistently formulated eddy-viscosity coefficient for k-equation model. Journal of Turbulence, 19(11-12):959- 994; 2019. https://doi.org/10.1080/14685248.2019.1567926.

Rahman MM, Miettinen A, Siikonen T: Modified SIMPLE formulation on a collocated grid with an assessment of the simplified QUICK scheme. Numerical Heat Transfer, Part B, 30(3):291-314; 1996. https://doi.org/10.1080/10407799608915084.

Rahman MM, Siikonen T, Miettinen A: A pressure-correction method for solving fluid flow problems on a collocated grid. Numerical Heat Transfer, Part B, 32(1): 63-84; 1997. https://doi.org/10.1080/10407799708914999.

Schlatter P, Orlu R: Assessment of direct numerical simulation data of turbulent boundary layers. Journal of Fluid Mechanics, 659:116126;2010. DOI: 10.1017/S0022112010003113

Segalini A, Orlu R, Alfredsson PH: Uncertainty analysis of the von Karman constant. Experiments in Fluids, 54:1460, 2013. DOI: 10.1007/s00348-013-1460-3

She Z-S, Chen X, Wu Y, Hussain F: New perspective in statistical modeling of wallbounded turbulence. Acta Mechanica Sinica, 26(6):847-861; 2010. DOI: 10.1007/s10409-010-0391-y

She, Z-S, Chen X, Hussain F: Quantifying wall turbulence via a symmetry approach: a Lie group theory. Journal of Fluid Mechanics, 827:322-356; 2017. DOI: 10.1017/jfm.2017.464

She Z-S, Hu N, Wu, Y: Structural ensemble dynamics-based closure model for wall bounded turbulent flow. Acta Mechanica Sinica 25:731-736;2009. DOI: 10.1007/s10409-009-0282-2

Townsend AA: The Structure of Turbulent Shear Flow, 2nd edition,1976. Cambridge University Press.

Wilcox DC: Turbulence Modeling for CFD, vol. 2. La Canada, DCW industries (2006).

MIJST
MIST International Journal of Science and Technology

Computational Design Approach to Re-Establish the Urban Fabric of Mongla: A Perspective from Grasshopper

Sumaiya Binte Azad

Department of Architecture, Bangladesh University of Engineering and Technology (BUET), Dhaka, Bangladesh

email: *sumjui51@gmail.com*

ARTICLE INFO

Article History:

Received: 08th September 2021
Revised: 21st November 2021
Accepted: 23rd November 2021
Published: 23rd December 2021

Keywords:

Mongla urban design
Computational urban design
Grasshopper-Physarealm modelling
Urban fabric

ABSTRACT

The Padma Multipurpose Bridge Project is the genesis of some subsequent projects in Bangladesh among which developing Mongla Port is one of the priority values. Since Mongla is an integral part of southern Bangladesh, the government has taken initiatives to integrate the port uses for neighboring countries. An agreement was signed (Intra Bangladesh, Butan, India, and Nepal (BBIN) Trade) for offering multi-modal transit access to India and Port access to Nepal, Bhutan and Eastern India. The objective of this study is to establish a computational way to analyze the existing fabric and restore a potential optimized fabric. The methodology of this study includes developing a computational approach, collecting data from secondary sources, analyzing the data set and adjusting it to the identified existing urban fabric. In this paper, a new tool is introduced named 'Physarealm', based on the algorithm of Grasshopper and Rhinoceros.

1. INTRODUCTION

Since the existing condition of communication infrastructure of Mongla port from the capital Dhaka as well as the borders is not up to the mark; the government of Bangladesh has set a new embellishment for the transportation system in southern parts of the country. According to the pre-feasibility report Mongla Economics Zone Bangladesh, the city economy was developed based on the port-oriented trade which was the main Central Business District (CBD) not only of this particular zone but the whole southern part of the country. Mongla could be referred to as a 'secondary city' in a developing country like Bangladesh which plays an explicitly influential position in regional economies. Besides, this city not only moulds the livelihood character of its urban residents but the working people of the industrial units within and around the district.

This research will demonstrate a new way towards a 2-dimensional systematic proposition instead of an analogous thinking approach and analyse the existing as well as a potential urban fabric of the Mongla port area. In recent times, the parametric design process is such a structured approach that evaluates a design via algorithm and ensures minimal assessment time while providing data accessible throughout the development phase (Motta, 1999). Designing has been a crucial aspect of our life; for years, perception of design sometimes has failed and some approaches have devastated both financial and physical resources. In addition, intuition sometimes could be misleading and strenuous whereas computer-aided programs could lend support in complex and comprehensive experimental analysis (Mawla *et al.*, 2018). Computer-aided designs can also perform in multitudinous directions at a time like- density, population, environment, energy, integration, material, distance, speed, time, demand etc.

On the account of Bangladesh endeavouring to establish a Digital Bangladesh programme, 'Smart city Campaign' has been launched recently. This project aims to emphasize improved urban environment and decentralization of facilities. These include the improvement of urban infrastructure such as vehicular and pedestrian connectivity, sewerage system, waste management, drinking water, energy-efficient techniques, community-level infrastructure. According to the authority, urban areas are the engines of economic growth and so the authority aims to develop economic corridors to integrate industry, infrastructure, urban services, institutional and regulatory framework (Acharjee, 2020).

Computational designs can lead to a future that minimizes rational errors. This study helps to relocate the existing bus and water terminal under the concept of Transit Oriented Development (TOD), considering the land use and other Infrastructure facilities in terms of land use pattern, existing urban fabric, transportation, environmental consideration, and last but not least, the physical and visual

accessibility to and from the stations.

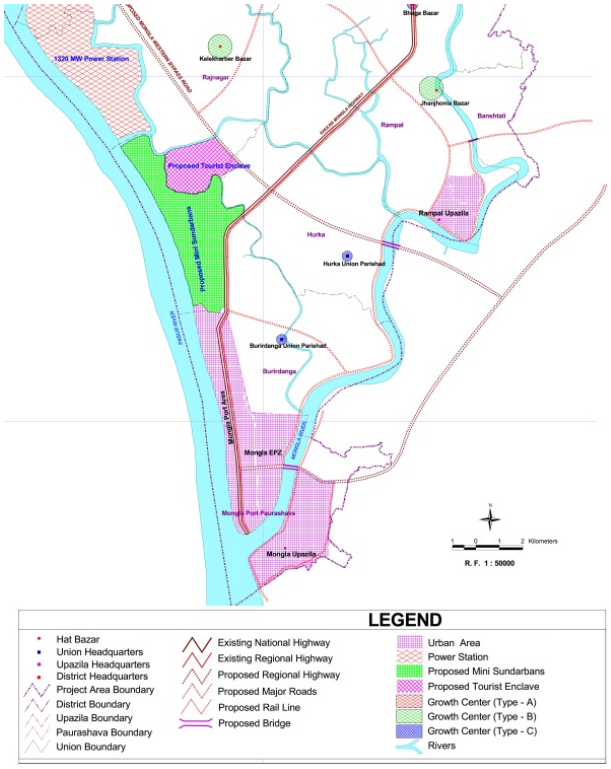

Figure 1: Land use pattern of Mongla Port Paurashva

2. COMPUTATIONAL DESIGN APPROACH

By 2050, there is a probability that 70% of the world's population will start living in megacities which indicates a mass of 10 million citizens. This data depicts that, there should be a whole new target-oriented, interdisciplinary programmed and well-structured approach in urban planning and design in cities (Renner, 2018). Subsequently, planners from across the world are tending to adopt computational methods. Accordingly, the presented framework depicts that, the use of digital tools and programming methods can be used for extensive research experiments while the outcomes can be computed in no time. A methodical algorithmic approach undoubtedly increases planning efficiency and variety at the same time.

3. EXISTING URBAN FABRIC

Figure 2: a, b, c, d from left to right; existing bus and water terminal

In the existing condition, an expiring bus stand and moribund water terminal works as the multi-modal transportation hub for years featured in Figure 2(a, b, c, d) as well as public transport is almost non-existent in Burirdanga UP & Mongla Port Paurashva. The EPZ alone offers 611 employment opportunities per hectare (total EPZ area is around 205 acres/83 hectares approx.). The existing fabric is pretty much fragmented and the spatial segments are isolated in terms of connectivity and infrastructures. The existing urban fabric can be divided into three grids; they are:

A. The connectivity grid

Connections and accessibilities of the area, which include vehicular roads, pedestrian networks, cycling tracks, etc.

B. The activity grid

Consists of public zones, residential zones, facility zones, service areas.

C. The green infrastructure grid

Comprises open public spaces, green networks, retaining water bodies, urban sprawl, permeable pavements, green roofs, trees and tree boxes, and rainwater harvesting systems.

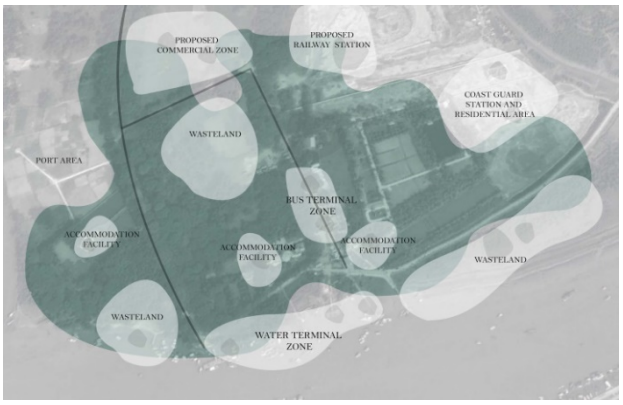

Figure 3: existing urban fabric

4. LITERATURE REVIEW

As discussed earlier, research has been conducted worldwide on computational urban planning and its spatial attributes. However, a research gap remains on Mongla, the city is one of the flourishing cities of Bangladesh which is not only the gateway to the Sundarbans but—constituents second largest seaport, export processing zone, power plant, fishing, and many other private industrial zones. According to Feisal and Kuhl (2021) Mongla has the potential for positive transformation of secondary cities. Parametric modelling authorizes engendering extensive urban design permutations that resemble sustainable design development targets.

So far, there are several computational methods and tools available for indirect urban fabric analysis, such as space syntax (Conroy-Dalton & Bafna, 2003), Isovists analysis (Batty, 2001), density-based quantitative analysis (Hausleitner, 2010), and Rhinoceros based plugin Grasshopper (Schneider, Koltsova, & Schmitt, 2011).

Rapid urbanization sometimes endangers many historical precincts with indigenous characters disappearing, present scenario of China indicates an urban fabric crisis (Ruan & Gu 2004). Modern cities undergo both energy problems (Polsky, 2014) and fragmentation caused by isolated building pattern, communication networks, and negative spaces (Trancik, 1986), converting the buildings into random pieces. Therefore, urban fabric assessment is considered as the cardinal aspect for developing a smart city (Li. 2016). It is also argued that the visual exposure of urban space which includes -buildings, public space, road network, differentiates cities from others (Proshansky, Fabian and Kaminoff, 1983). In short, proper urban fabric planning and design is the paramount objective for a smart city.

The emergent trait of swarms and self-organizing attributes have turned them into popular appliances among architects of the computational field, as well as their strategic approach against complexity and the diversified possibility they comprise (Pantic & Hahm, 2015). A team of Japanese and Hungarian researchers has shown that *Physarealm* can find the shortest route between two food sources when set in a maze with two oatmeal flakes (Nakagaki et al. 2000). In a survey from 2010, *Physarealm* created a network similar to the existing routes of the train system of the Tokyo area (Tero et al. 2010). Since then, researchers have been using Physarealm modelling for the spatial formation study and to apply architecture-planning sectors.

5. OBJECTIVES

The goal of the study is to develop an intelligent transportation infrastructure of the area through computational progress for the betterment of local people, to provide the commuters a convenient as well as congenial walking courses, to create a buffer yet easy access among all terminals, reducing walking distances in between the terminals and eliminating passenger - vehicle conflict points, designating particular areas for services and finally, increasing the number of existing facilities.

6. COMPUTATIONAL METHODOLOGY

A. Addressing the algorithm

Software - Rhinoceros 3D is popular commercial Computer-Aided-Design software developed by Robert McNeel & Associates for designers, architects, planners which is based on fundamental programmed geometric parameters. A Rhinoceros-based plugin 'Grasshopper' is used to create a prototype of a circulation pattern. 'Physarealm' is an agent-based stigmergy algorithm modelling, programmed on *Physarum Polycephalum* and similar to the ant colony algorithm. *P.Polycephalum* is a slime mold that inhabits shady, cool, moist areas such as decaying leaves and logs.

The presented model reproduces the biological behaviour of *Physarum*; which are formation, growth and minimized transport networks. We can delineate the basic pattern from these simulation outcomes by simplifying them. Hereby, we can find different shapes of routes chosen by slime by connecting several nodes. Several trails were extracted from the generated slime movement patterns time to time.

B. Computation process

The site is located near the Mongla port. If the TOD radius is taken as 1 km according to the standard of the Dhaka Mass Rapid Transit Development Project (TOD) Report, the possible outcome is shown in Fig.3a. However, the existing bus and water terminal lies right next to the upcoming railway station.

The simulation was run several times based on different parameters like - population, density, speed, and flexibility. The result was fascinating which could be portrayed as a basic physical pattern.

Step1. Assessing the survey data and integrating with Grasshopper and Physarealm.

Step2. Place Physarealm and connect the primary data set with it- like environment (surfaces, geometry, and boundary), emitter points, foods, population etc.

Step3. Set up the additional settings like- Chemo field, death-birth rate, angles, etc. and run the simulation for 3-4 hours until it achieves stability.

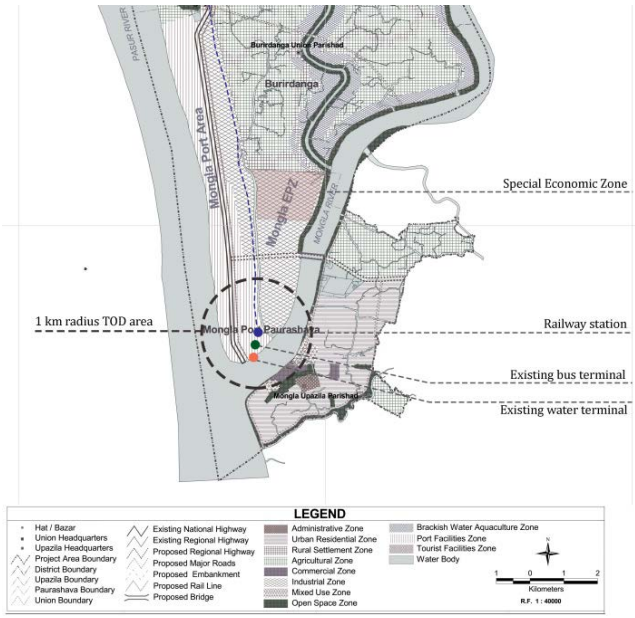

Figure 4: Land use pattern of TOD area and surroundings

C. Tools

Rhinoceros is primarily an organic surface modeling system that utilizes the NURBS mathematical model. Rhinoceros incorporates specific fields such as rendering and animation, architecture and planning, engineering, prototyping, and others. The integrated plugin tool- 'grasshopper' allows parametric measures for design proposal which runs different kinds of simulations and experiments. Recently, in the contemporary architecture field, Grasshopper is one of the most premier programming engines for planners, exceeding in networking, urban planning, digital fabrication, generative art, simulation depending on numeric, geometric, visual variables. It has become user-friendly not only due to its high flexibility but efficiency and swift exploratory experiences as well.

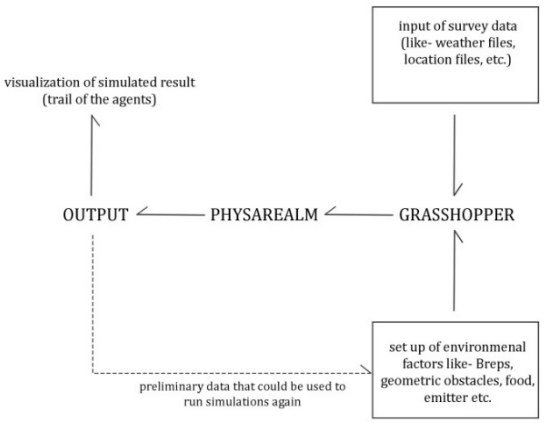

Figure 5: workflow with Physarealm.

The apparatuses are:

Environment: Contains the eps file of the particular environment and location, comprises 3D modeling atmosphere. The agents can move at any orientation in the 3D lattice-based model. The eps file is integrated within the modeling with a Brep container which operates in 3D orientation.

Obstacle: Users can assign physical obstacles as Breps within the grid as well as a barrier aligned with the site line. A customized high escape possibility may manipulate the regulations and allow the agents to enter obstacles. In this study, an old mosque plaza (local landmark), a chunk of old trees and a canal were maintained as obstacles in the last four scenarios. Apart from that, for the first two simulations, the surface was maintained as barren land.

Surface: A defined 2D or 3D surface area to start with, performs perfectly for either file- Brep or geometric shapes.

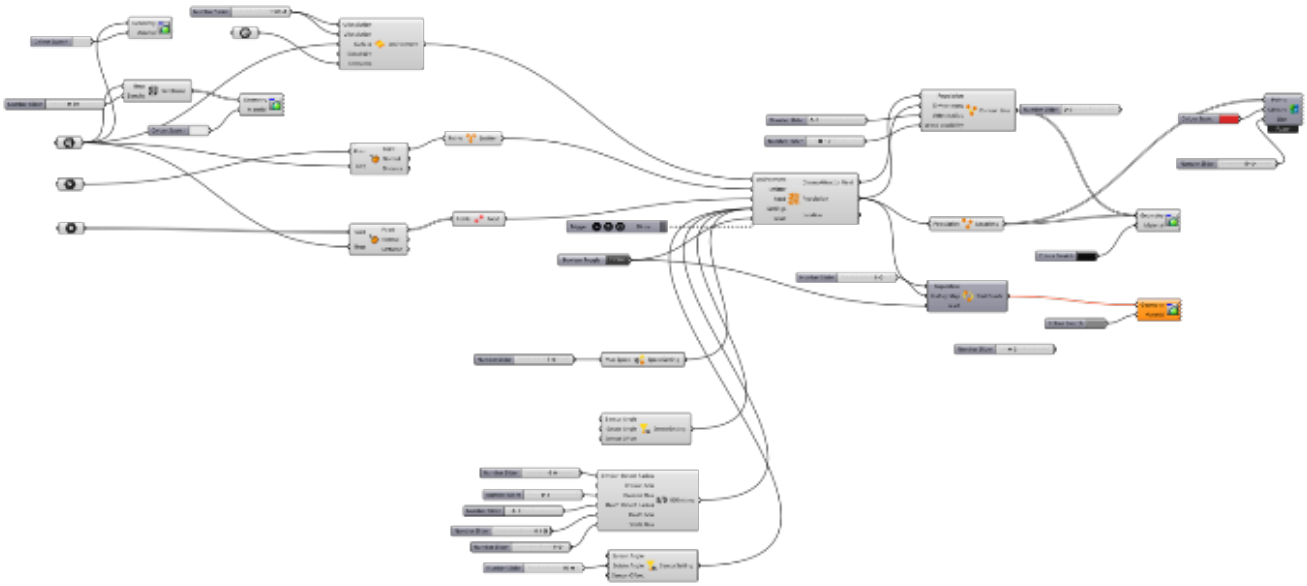

Figure 6: Environmental parameters from Physarealm

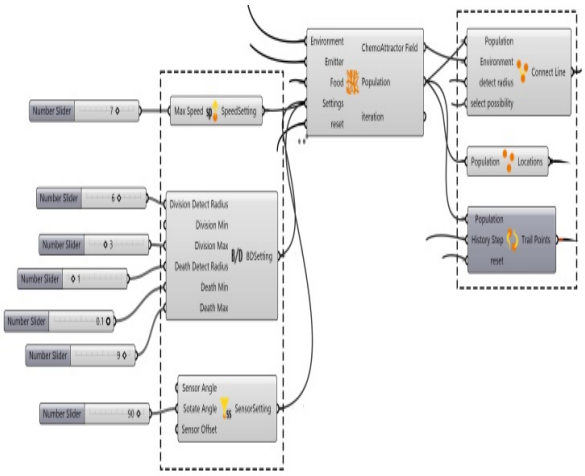

Figure 7: parameters from Physarealm

Emitter: A set of point containers, generate agents near the specified locations and provide them random orientations. The bus terminal, railway station, water terminal etc. could serve as the emitters since people are dispersed from these hubs.

Food: Serves as the destination of the agents. These sets of points constantly emit chemo-attractive trails to attract the agents. The foods could represent the destination points e.g. public plazas, accommodation facilities, commercial zones, market spaces, residential areas etc. 'Food' provokes the agents to find a way among them in terms of minimized walking distance and time.

The additional settings are: Speed max. 7~10, sensor angle 0, 30, 60, 90, detect radius 5~8, division max 3, death radius 1~3, death min0.1~0.3, death max 6~9, sotate angle 90.

The output variables are:

Chemo attractor field: Attracts the agents depending on the value given. Every agent has multiple sensors to detect the level of chemo-attractive trail concentrations in front of it. This could represent the techniques like signboards,

digital direction boards, etc.

Population: Number of agents to experiment with, in this case between 100- 300.

In addition, added values of birth-death rates (5-10), sensor angles (multiple of 30) in the settings, happen to manipulate the outcome. The live formulation and growth of the programmed mold can be supervised in grasshopper which leaves some trails according to the movement of the agents. The 'trail point' is the rudimentary pattern developed by the agents which depict the minimal distances among the destinations of the algorithm.

Possibility range 0.1~0.3, detect radius 0~2, history step 5~9, Boolean Toggle and reset button attached to reset option to operate independently.

D. Analysis and interpretation

In the figure shown in 5a, we can observe the raw trails constructed at several time-lapse which were manipulated by the measures described before.

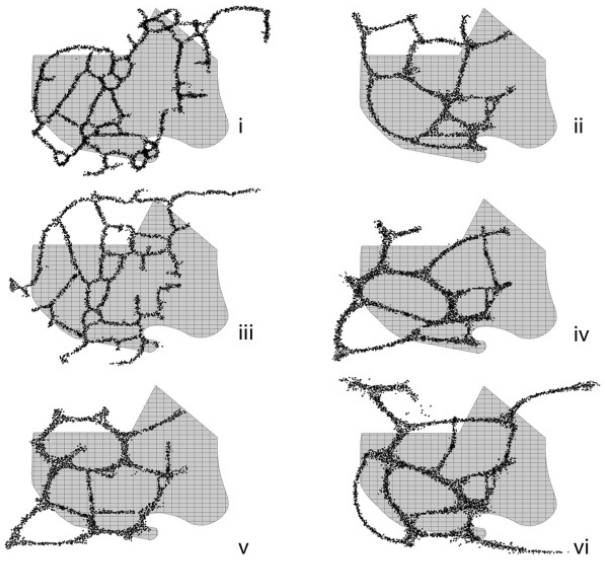

Figure 8 : sample simulation patterns from Physarealm

To the best knowledge, after gathering a good number of samples (at 4-5 hours per run), a simplified pattern was generated. Some sample patterns shown in Fig 5a, represent common specimens which are shown in Fig. 5b. At first, the simulation trails were simplified and the food nodes were identified. The trail curves were traced with digital media and at last, the simplified lines were inferred.

The simplified reference wireframe paves the way to propose some major changes in connectivity. The simplified traced trail sets were again stacked on each other and a sketch was delineated. In Fig.6, we can see the simplified connection grid according to the computational design process. The proposed grid results in several fragmented zoning which could serve as urban buffer spaces. The foods are represented by dots and the dotted lines symbolize the minimal distance trail patterns from the simulation.

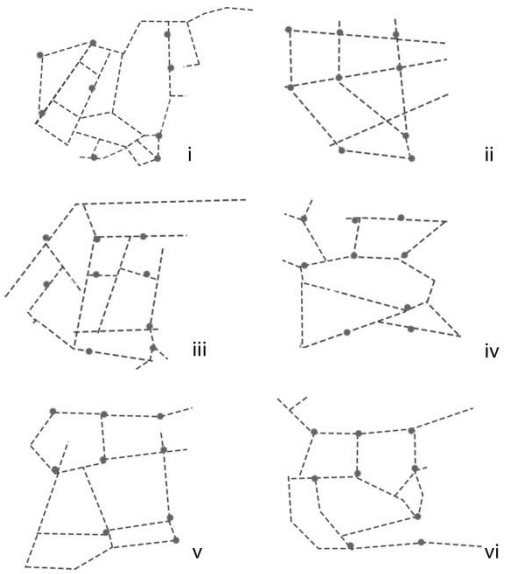

Figure 9: simplified patterns from simulations

7. OVERVIEW AND VISUALIZATION

We can delineate a basic trail from the generated simplified patterns which are shown in Fig. 6. The fundamental sketch depicts that, the grid should be something like this.

- railway station
- bus terminal
- water terminal
- port area
- riverfront areas

The final output of the calculation modifies the three major grids:

- The connectivity grid – vehicular and pedestrian connections and accessibility.
- The activity grid – public spaces and facilities, accommodations.
- The green infrastructure grid – green network which serves as natural urban buffer spaces.

a. Port facility zone – proposed in KMDP development management plan 2011-2031, situated in between the river and railway station.

b. Railway station plaza – connected with the N7 highway via proposed connecting road (ii & iii/Figure 6).

c & f. Economic district – Proposed EPZ and special economic zone.

d. Urban buffer zone – consists of existing forest office, accommodation facility and coast guard station at present. The proposed urban zone should be enriched with natural resources, green landscape and waterscape.

e. Bus terminal zone – situated in the existing bus stand area, the capacity and efficiency should be maximized.

g. Public recreation zone and accommodation zone – located in the area of existing urban open space at present. Riverfront development is suggested like – boat club,

cycling and pedestrian tracks, sitting arrangements etc.

h. Water terminal zone – the terminal should be upgraded with modern amenities and facilities since this is one of the main access points of the world's largest mangrove forest, the Sundarbans. To promote tourism, there is no other option but to improve the connectivity grid.

i. Coast guard station and forest office – is suggested to be relocated to this zone since zone 3 and 5 are potential sites for urban breathing with huge natural resources.

A. Connectivity grid

The access points to the site are:

- N7 highway extension
- Proposed approach road to EZ
- Proposed connecting road to the bypass road.
- Proposed one-way connection towards the bypass (through the hub to maintain a loop)
- Proposed one-way road to complete a loop.

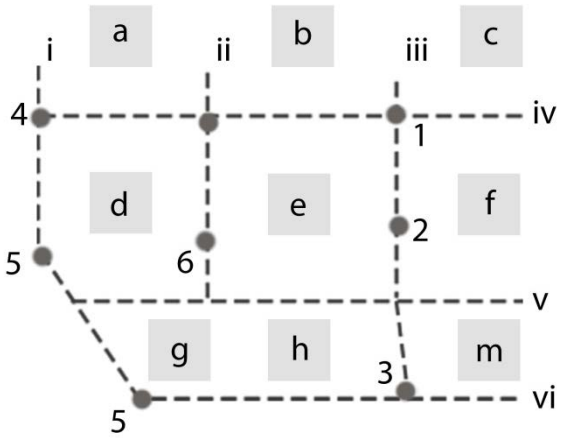

Figure 10: Proposed non-vehicular access.

B. Activity grid

Public plazas can be placed tactfully to define different zones and to avoid any chaos which may serve as urban buffer spaces place to place. In this case, the public recreation zone is consistent with the existing condition which works perfectly, optimized by the public itself.

The riverbank development area offers visitors to enjoy the sublime beauty of the confluence, which is situated at the dead-end of the N7 highway, right beside the port premises. The complementary composition of the riverbank, the sunset on the horizon along with incoming ships towards the port, offers a majestic atmosphere. This zone may be developed as public recreation zone with modern facilities and amenities. The portside plaza offers a vast natural landscape for public amusement and facilities like- exhibition, public gathering, amphitheatre, cycling track, outdoor sports ground, early development, youth entertainment, family and friends, pet corner, gym area etc. It is situated not so far from the terminals so; the visitors or tourists can always make a little escape from the hectic long run. The plaza is well distinguished from the water terminal and the bus terminal by the accommodation facility zone, shown in Figure 7.

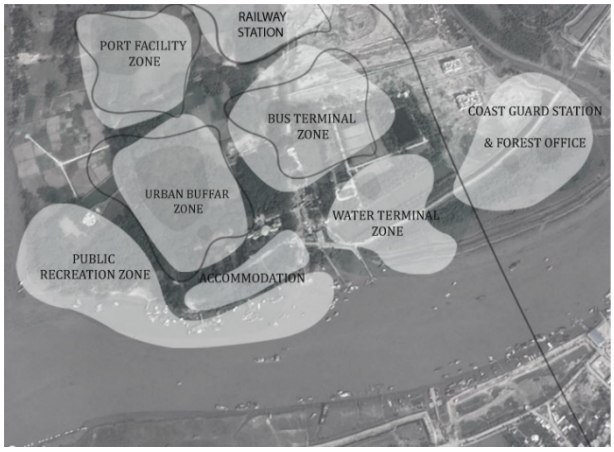

Figure 11: visualization of proposed urban fabric

The existing accommodation facility may be enriched by developing the neighbourhood recreation zone. This facility area separates the central urban zone and the riverbank plaza.

C. Green infrastructure grid

Zone d - The buffer area should be used as an urban green space to check the chaos and sound between the hub and the rest of the zones. The quality may be enhanced by a natural preservation program along with basic infrastructural systems which include sitting arrangement, rainwater reservoir, stormwater swale, retention drains, pedestrian and cycling tracks etc. This new chunk may be stretched out through the medians and pedestrian networks and connect with other green chunks.

8. CONCLUSIONS

Once the prototype analytical file is set up, the evaluation and simulation could be easily manipulated for further innovation. From this study, we can negotiate that there are further possibilities in terms of zoning and connectivity in Mongla port area. A new way can be portrayed the extended connectivity grid and the activity grid as well from this computer-aided design study. Physarealm-Grasshopper has been used in urban connectivity and morphology, parametric landscape and digital fabrication at large. A park pathway is established based on Physarealm, among several sports facility premises congregated by an Olympic stadium (Yidong, 2017).

In short, the presented framework depicts that the use of digital tools and programming methods can be used for extensive research while the outcomes can be computed in no time. The computational approach undoubtedly increases the planning efficiency and variety at the same time. The work with the parametric plug-in Grasshopper offers comprehensive and user-friendly approaches in the generation of various designs.

Once the computational linguistics is achieved data interpretation and schematic plan can be ended in a very short period of time along with the digital fabrication of the whole design process. This suggested wireframe reveals a highly potential experimental program that could take months to reach up to this point. In this age of modernism and advanced technology, computational

design process is the most methodical and productive perspective.

Future study will concentrate on the absolute 3-Dimensional formation of morphological features hopefully due to the intricate survey study and extensive methodology.

REFERENCES

Acharjee Deepak, (2020), The Independent, February 5th, Four metropolitan cities to turn into 'smart cities' Rhinoceros 3d application. Source: https://en.wikipedia.org/wiki/Rhinoceros_3D, Extracted on July 21, 2021.

Apps for Rhino and Grasshopper, Source: https://www.food4rhino.com/en/app/physarealm, Extracted on July 21, 2021.

Batty M., (2001) ''Exploring isovist fields: Space and shape in architectural and urban morphology,'' Environ. Planning B, vol. 28, no. 1, pp. 123–150.

Conroy-Dalton R. & Bafna S., (2003) ''The syntactical image of the city: A reciprocal definition of spatial elements and spatial syntaxes,'' in Proc. 4th Int. Space Syntax Symp., pp. 59.1–59.22.

Detailed Area Plan [Mongla] Port Paurashva DAP.

Executive summary draft: pre-feasibility report Mongla Economics Zone Bangladesh/pp 32-33

Fink T., Koenig R. (2019), Data - city information modelling and GIS - Volume 3 - eCAADe 37 / SIGraDi 23, pp 313

Hausleitner B., (2010) ''Tracing scopes of action. Approaching the complexity of the urban block,'' M.S. thesis, EMU, Delft, The Netherlands.

Koenig R., Knecht K., Buš P., (2017) Koenig R. et al "Interactive Urban Synthesis- Computational Methods for Fast Prototyping of Urban Design Proposals".

Li X. et al. (2016): Assessment of Urban Fabric for Smart Cities.

Mawla A.,Schneider S., Bielik M., Koenig R. (2018), Integrated Data Analysis for Parametric Design Environment, mineR: a Grasshopper plugin based on R 36th eCAADe Conference - Computing for a better tomorrow pp. 320

Motta, E 1999, Reusable Components for Knowledge

Modelling: Case Studies in Parametric Design Problem Solving, IOS Press.

Nakagaki, T., Yamada, H. and Toth, A.: (2000), Intelligence: Maze-solving by an amoeboid organism, Nature, pp. 470-470.

Pantic, I. and Hahm, S.: 2015, Isomorphic Agency, Emerging Experience in Past, Presentand Future of Digital Architecture, Proceedings of the 20th International Conference of the Association for Computer-Aided Architectural Design Research in Asia CAADRIA, pp.178-188

Polsky C. et al. (2014), ''Assessing the homogenization of urban land management with an application to US residential lawn care,'' Proc. Nat. Acad. Sci. USA. vol. 111, no. 12, pp. 4432–4437,

Pre-Feasibility Report-Mongla Economic Zone, Bangladesh. (2015), pp 139-140.

Proshansky H. M., Fabian A. K., and Kaminoff R., (1983), 'Place-identity: Physical world socialization of the self,' J. Environ. Psychol., vol. 3, no. 1, pp. 57–83.

Rahman f. & Kuhl L. (2021) "Putting Mongla on the Map: The Curious Case of a Coastal Secondary City's Transformation". In United Nations Research Institute for Social Development. Source: https://www.unrisd.org/transformation-mongla, Extracted on July 20, 2021.

Renner, R (2018), Urban Being, Anatomy & identity of the city, Salenstein.

Ruan Y., and Gu X., (2004) ''An analysis about the practical patterns to conserve the historic districts in China,'' J. Tongji Univ. Soc. Sci., vol. 15, no. 5, pp. 1–6.

Schneider, C., Koltsova A., Schmitt G, ETH Zurich. (2011) "Components for Parametric Urban Design in Grasshopper. From Street Network to Building Geometry"/pp 68

Spring Simulation Multi-conference, SpringSim '11, Boston, MA, USA.

Status paper on Asian highway Bangladesh (2011), Roads Division, Ministry of Communications Bangladesh.

Tero, A., Kobayashi, R. and Nakagaki, T.: (2007), A mathematical model for adaptive transport network in path finding by true slime mold, Journal of theoretical biology, pp. 553-564

The Preparatory Study on the Dhaka Mass Rapid Transit Development Project (TOD), Final Report, pp-3_158

Trancik R., (1986), Finding Lost Space: Theories of Urban Design. New York, NY,

Volume 8: Proceedings of the 2011 Symposium on Simulation for Architecture and Urban Design (SimAUD).

Yidong M., Weiguo X., (2017), Proceedings of the 22nd International Conference of the Association for Computer-Aided Architectural Design Research in Asia (CAADRIA) 2017, pp 499-509.

MIJST
MIST International Journal of Science and Technology

Performance Analysis of a Low Head Water Vortex Turbine

Badhan Saha[1*], Mazharul Islam[2], Khondoker Nimul Islam[3], Jubair Naim[4], and MD Shahriar Farabi[5]

Department of Mechanical and Production Engineering (MPE), Ahsanullah University of Science and Technology (AUST), Dhaka, Bangladesh

emails: *[1]badhan.mpe@aust.edu; [2]mazharul.islam.mpe@aust.edu; [3]foysalkhondoker@gmail.com; [4]jubairnaimakash9854@gmail.com; and [5]shahriarfarabiw30@gmail.com*

ARTICLE INFO

Article History:

Received: 04th May 2021
Revised: 18th November 2021
Accepted: 20th November 2021
Published: 23rd December 2021

Keywords:

Water vortex turbine
Micro hydro power
Renewable energy

ABSTRACT

A small hydropower plant is an environment-friendly renewable energy technology. The run-of-river type gravitational water vortex turbine can be designed to produce electricity at sites with low water heads. In this study, an experimental investigation was undertaken on this type of turbine with a water tank and a runner which is connected to a shaft. At the end of the shaft, a rope brake was attached to measure the output power, torque and overall efficiency of the vortex turbine by varying flow rates. The designed vortex turbine can achieve an overall efficiency of 52.67%. The experimental results were validated with available data in the literature and theories associated with the turbine. The results also showed that the flow rate plays a vital role in generating power, torque as well as overall efficiency. The project was completed using local resources and technologies. Moreover, as water is used as the input power, this project is eco-friendly which has no adverse effect on the environment.

1. INTRODUCTION

A micro-hydropower plant like a low head gravitational water vortex power generation system can be installed in prospective sites to generate pollution-free electricity. The water vortex turbine, as shown in Figure 1, is a simply constructed turbine that can produce electricity using water flows. The turbine is placed into a conical basin where the vortex is generated. When water is introduced into a conical basin tangentially, it creates a vortex and energy is harnessed. The blades of the turbine can be straight or curved. A dynamo can be coupled with the shaft of the turbine to produce electricity.

A two-dimensional representation of the experimental setup of the vortex turbine has been shown in Figure 2. In Figure 2 (a), various parts have been incorporated and in Figure 2 (b), the dimensions of various parts of the vortex turbine have been presented. Figure 3 shows the three-dimensional CAD drawing and Figure 4 shows the actual experimental setup of the vortex turbine with various parts.

Austrian engineer Frank Zotloterer invented different types¨ of Gravitational Water Vortex Power Plant (GWVPP) which has the potential to generate power using low head (ZOTLÖTERER, 2011). According to (Ersoy, 2014), Hakim investigated the effect of distances between oscillating parts in a vortex-induced power generation. Permana (Permana, 2011) studied the effect of the free surface on the oscillating part involving the performance of a vortex turbine. He found that the lower the location of the oscillating part, the greater the amplitude of the water level and vice versa. This finding is due to many reasons and one of which is the holder stability.

Bernitsas and Raghavan (Bernitsas *et al.*, 2006) designed a vortex-induced vibration aquatic clean energy (VIVACE) converter which used ocean/river current hydrokinetic energy for the first time. Punit Singh and Franz Nestmann (Singh & Nestmann, 2009) designed an optimized water-free vortex propeller runner for micro-hydro application and conducted experimental investigations.

Piyawat Sritram and Ratchaphon Suntivarakorn (Sritram & Suntivarakorn, 2017) showed a comparison between the water-free vortex turbine and the small undershot water turbine. They (Sritram & Suntivarakorn, 2017) found that the highest efficiency of a waterfree vortex turbine was 35.92% at the rotational speed of 50 rpm and the torque was 2.77 N-m. The output power of their turbine was 14.5 W.

Recently an experimental investigation has been carried out by Saleem *et al.* (A.S. Saleem *et al.*, 2020) to investigate the various performance parameters of gravitational water vortex turbine (GWVT) by varying design and flow conditions. They have shown that to get better performance from (GWVT), the vortex height and vortex shape have been played an important role. They have also suggested that the better performance of the

GWVT can be found at the middle range of rotational speed. They have found that the multistage GWVT has produced more power than single-stage GWVT. Rahman *et al.* (Rahman *et al.*, 2018) have performed an experimental investigation Ullah *et al.* (Ullah *et al.* 2020) have performed an experimental investigation on multistage GWVT using savonius type blades and telescopic shafts to investigate the effects of various parameters on the performance of GWVTto study the effects of inlet flow rates on the performance of GWVT. They have shown that the efficiency of the GWVT has been increased when the inlet flow rate has become higher. Moreover, they have found greater efficiency as well as power with large deflector length and small penstock's feeding width. Bajracharya *et al.* (2020) have performed numerical and experimental investigations to reveal the effects of geometrical parameters on the performance of GWVT. From their experimental and numerical analysis, they have suggested that when designing a turbine runner, the height of the runner should be considered as the most significant parameter.

In the present research, the main focus was to fabricate a small-scale vortex turbine and to test the performance at different operating conditions.

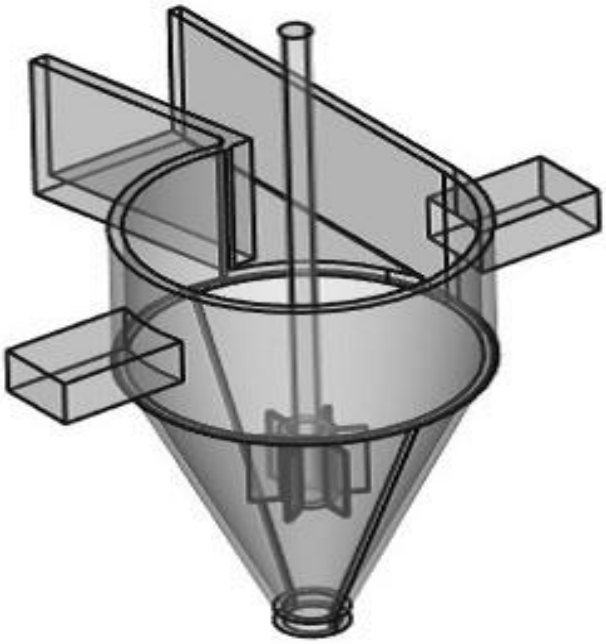

Figure 1: Illustration of a Gravitational Water Vortex Turbine inside a Conical Chamber

2. MATERIALS AND METHODS

A. Main Components

An experimental setup was prepared for laboratory investigation using a vortex turbine, as shown in Figure 5. The main components of the experimental setup were:

- A water tank to supply water to the turbine
- A canal with a notch to increase the water velocity
- A conical basin to generate vortex
- A straight bladed vortex turbine with six blades with a diameter of 0.11 m to generate torque
- A centrifugal pump to return the water from the water tank to the canal
- A rope-brake dynamometer mechanism (GUPTA, 2012) to measure torque generated by the turbine
- A digital tachometer to measure the turbine rotational speed

The salient parameters of the experimental setup are illustrated in Figure 2 and a 3D representation of the setup is shown in Figure 3. The basin height of the setup is 0.375 m with an inlet diameter of 0.400 m and an outlet diameter of 0.0816 m. The canal height of the setup is 0.2 m and the total length is 1.47 m. The Notch Angle, shown in Figure 2, of the turbine, is 15 degrees and the cone angle, also shown in Figure 2, is 67 degrees. There were different types and angles of blade arrangements attached with the turbine. In this experiment straight bladed water vortex turbine was used that had six blades with a diameter of 0.11 m.

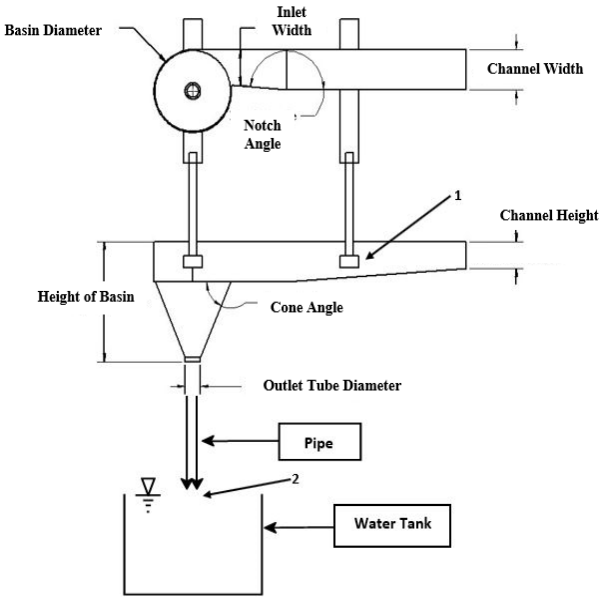

(a)

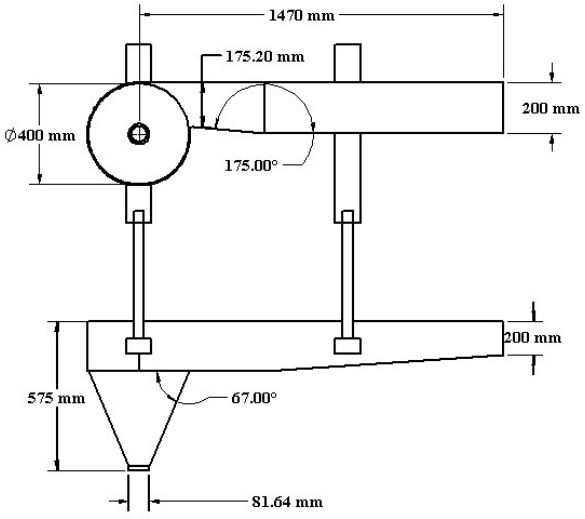

(b)

Figure 2: Experimental Setup in 2D with (a) various parts and (b) dimensions

B. Procedures

The experimental procedure is shown in Figure 5. Initially, water was fed from the water tank (shown in Figures 2 and 5) to the canal. The water flow was controlled by a ball valve, attached to the pressure gauge, manually. Then, the water was flowing through the flow meter and was delivered to the conical basin.

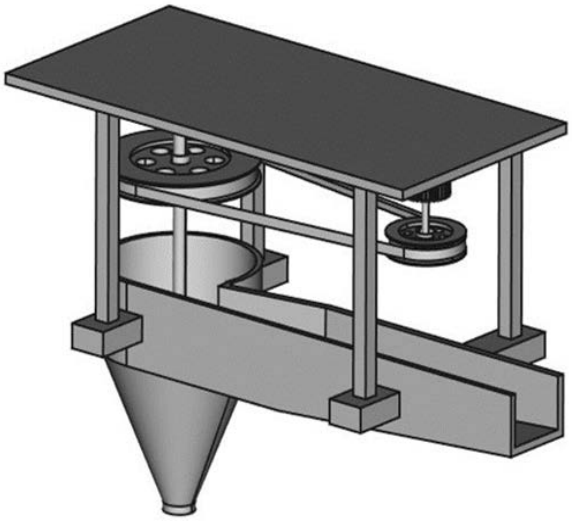

Figure 3: The Experimental Setup in 3D

In the conical basin, a vortex was generated due to its shape. This vortex impinged on the vortex turbine blades to generate the desired torque. One of the ends of the shaft was attached to the turbine and the other end was attached to a rope brake dynamometer. In the research, the flow rates of incoming water were varied between 0.000859 m^3/s to 0.00172 m^3/s. The variations of pressures were between 8618.45 and 89631.8 Pa.

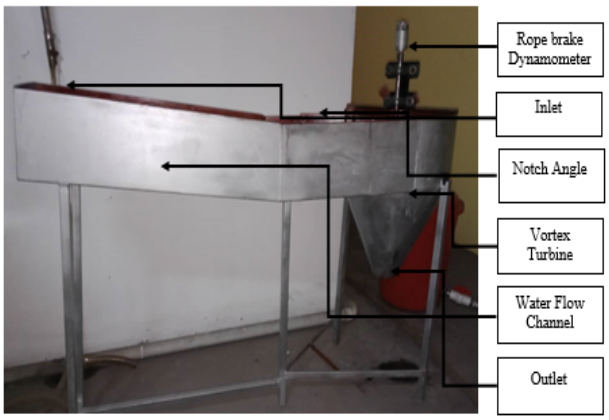

Figure 4: Picture of the Experimental Setup

The torque generated by the vortex turbine was measured by using a rope-brake system shown in Figure 6. The load was increased in the rope brake dynamometer to reduce the turbine rotation by adjusting the tension of the spring balances. The measured value of the highest rpm was 264 at 89631.8 Pa and the lowest rpm was 98 at 8618.45 Pa.

As this is a small scale project, the water pressure was confined to 89631.8 Pa, but on a larger scale project, it can be increased along with the flow rate. It was observed that the rpm increased with the increase of the water flow rates. The whole experiment was repeated by varying the flow rates and the data were measured several times to decrease uncertainties.

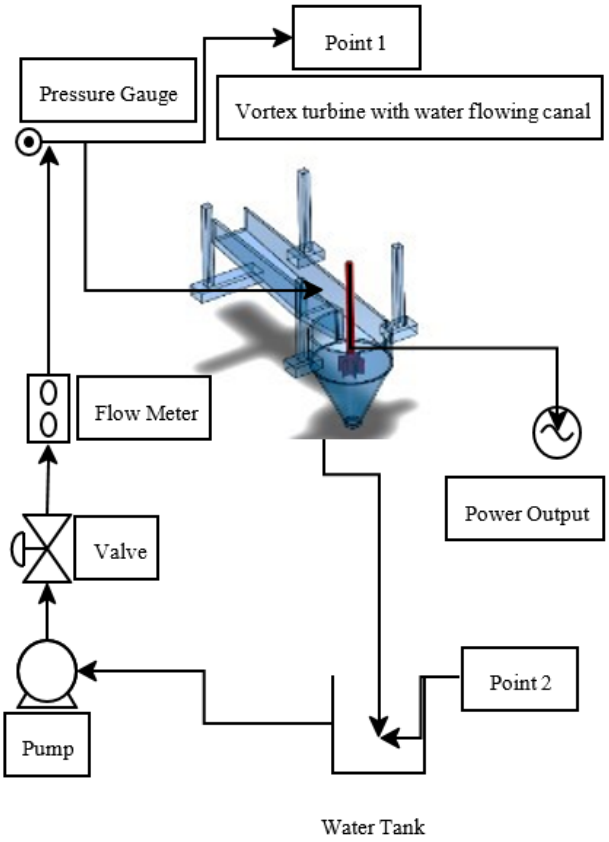

Figure 5: Methodology of the Experimental Investigation

3. MATHMETICAL EXPRESSION

A. Turbine Head

Applying Mechanical Energy Equation between points 1 and 2, as shown in Figure 5, we get (Çengel, Y., & Cimbala, J, 2014)

$$\frac{p_1}{\rho g} + \frac{v^2{}_1}{2g} + z_1 - h_T = \frac{p_2}{\rho g} + \frac{v^2{}_2}{2g} + z_2 - h_L \quad (1)$$

It should be noted that Pressure at points 1 (indicates the inlet) & 2 (indicates the outlet) are basically atmospheric pressures. As $v_2 \ll v_1$, v_2 can be neglected to simplify the equation. Also, the head loss term in the above equation (denoted by h_L) has also been neglected. Applying these assumptions, the above equation become.

$$h_T(m) = \frac{v^2{}_1}{2g} + \Delta Z \quad (2)$$

B. Flow Rate

$$Q = Av \quad (3)$$

$$v = \frac{Q}{A} = \frac{4Q}{\pi d^2} \quad (4)$$

C. Hydro Power

The hydropower available in the inlet of the vortex turbine (indicated by P_i) can be determined from (Çengel, Y., & Cimbala, J, 2014)

$$Pi = \gamma Q h_T \quad [W] \quad (5)$$

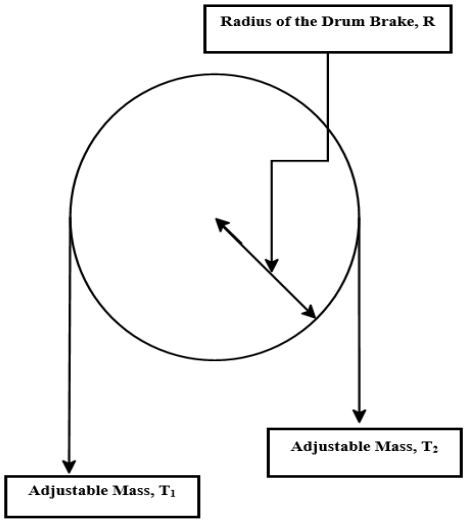

Figure 6: Schematic Representation of the Rope Brake Dynamometer

D. Output Power

The power generated from the vortex turbine (indicated by P_o) can be determined from the following expression obtained from (GUPTA, 2012)

$$Po = (T_1 - T_2) g \omega R \quad [W] \tag{6}$$

Overall Efficiency (η) can be expressed by

$$\eta = \frac{Po}{Pi} \times 100 \tag{7}$$

5. RESULTS AND DISCUSSION

A. Variation of Rotational Speed with Flow Rate

Based on the experimental investigation mentioned earlier, variation of flow rate with the turbine rotational speed is plotted and shown in Figure 7. From this figure, it was observed that with the increase of the flow rate, the rotational speed increased. It occurs because of gradual increase in the volume of water creates more pressure on the turbine blade. Hence the turbine rotates at a greater speed. The highest rotational speed in *rpm* was 264 at a flow rate of 0.00172 m^3/s . It should be noted that Sritram and Suntivarakorn (2017) obtained a similar trend and they showed that the rotational speed of a water vortex turbine increased with the increase of flow rates.

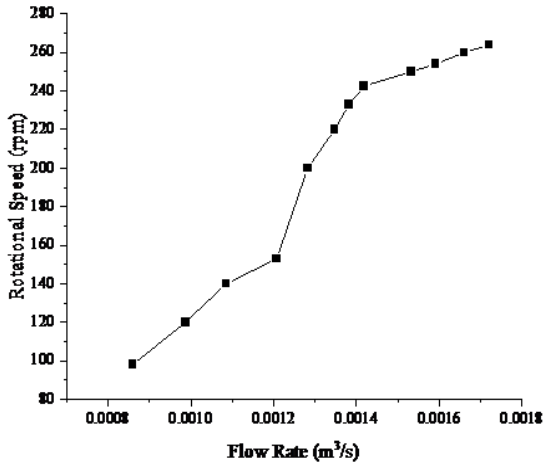

Figure 7: Variation of Flow Rates with Rotational Speed

B. Variation of Efficiency with Rotational Speed

Figure 8 shows the variation of efficiency with rotational speed. As the flow rate increases, the rotational speed and the corresponding efficiency of the water vortex turbine also increases. At the flow rate of 0.00172 m^3/s corresponding pressure was 89631.8 *Pa*. In that time the highest magnitude of efficiency has been found. The magnitude of the highest efficiency was 52.67% (at 264 *rpm*) and the lowest efficiency was 2.22% (at 98 *rpm*). Dhakal *et al.* (2017) showed the rpm versus efficiency curve in their experimental work, which is quite similar to the curve obtained in the present work.

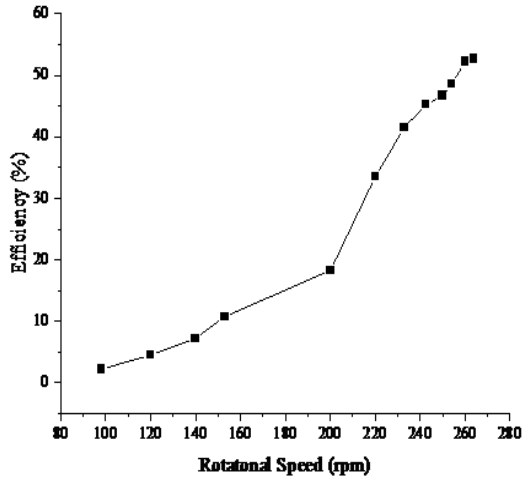

Figure 8: Variation of Efficiency with Rotational Speed

C. Variation of Rotational Speed with Flow Rate

Figure 9 shows the variation of output power with rotational speed. From this figure, it was observed that with the increase of the rotational speed, the output power also increased. This is due to the fact that as the rotational speed of the flow rate of 0.00172 $\boldsymbol{m^3/s}$ and pressure of 89631.8 *Pa*, the highest amount of output power (which was 12.3 *W*) was obtained at the rotational speed of 264 *rpm*. The lowest output power was 0.177 *W* at a rotational speed of 98 *rpm*.

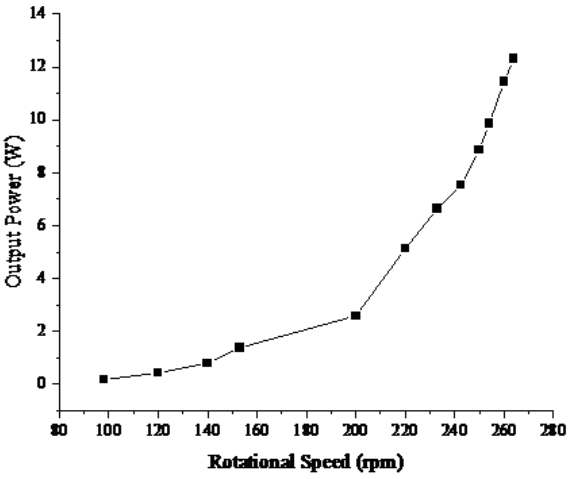

Figure 9: Variation of Power Output with Rotational Speed

D. Variation of Torque with Flow Rate

The variations of torque with flow rates are shown in Figure

10. It is seen that the torque increased with the increase of flow rate. As the flow rate increased, the corresponding volume of water is also increased. Different amounts of masses were applied to reduce the rpm and the corresponding magnitude of torque was recorded along with the rotational speed in rpm and flow rate. The maximum torque was 0.44538 *N-m* at a flow rate of 0.00172 m^3/s . The lowest torque was 0.0172 *N-m* at a flow rate of 0.000859 m^3/s.

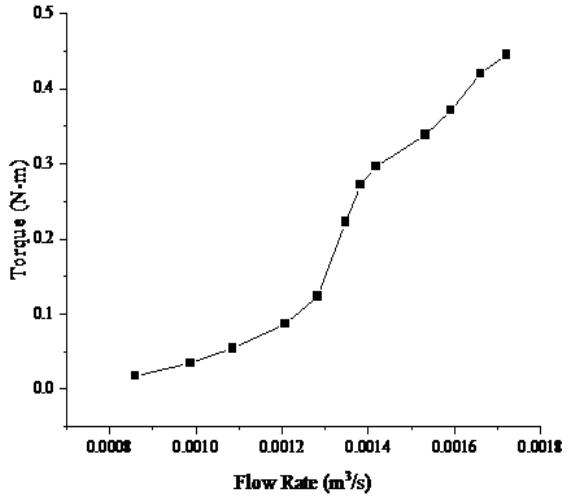

Figure 10: Variation of Torque with Flow Rates

6. CONCLUSIONS

A small-scale water vortex turbine with straight blades has been fabricated with the locally available materials and manufacturing facility in Dhaka for conducting experimental investigations. Experimental works were conducted with several important parameters related to the performance of a vortex turbine. It was found that as the flow rate increase, the rpm, output power and efficiency also increase. The generated output power was 12.3 *W* at a rotational speed of 264 *rpm* and the resulting efficiency was 52.67%. In future, a vortex turbine with curved blades may be investigated for higher efficiency.

7. NOMENCLATURE

D	Diameter of the nozzle
E_t	Turbine head
N	Rotational speed of the turbine in rpm
p_1	Pressure at point 1
p_2	Pressure at point 2
Q	Flow Rate
R	The radius of the brake drum
v_1	Velocity at point 1
v_1	Velocity at point 2
T_1	Adjustable mass # 1
T_2	Adjustable mass # 2
Z_1	Datum Head at point 1
Z_2	Datum Head at point 2
GWVPP	Gravitational Water Vortex Power Plant
VIVACE	Vortex-Induced Vibration Aquatic Clean Energy
VIV	Vortex-Induced Vibration
ω	Rotational speed in rad/s = $\frac{2\pi N}{60}$

ACKNOWLEDGMENTS

The authors are grateful to the Department of Mechanical and Production Engineering, Ahsanullah University of Science, and Technology (AUST) for the overall supports to carry out this project. A special thank goes to those who helped to complete this project.

REFERENCES

Alwan, H., & Al-Mohammed, F. (2018). Discharge coefficient for rectangular notch using a dimensional analysis technique. IOP Conference Series: Materials Science And Engineering, 433, 012015. https://doi.org/10.1088/1757-899x/433/1/012015

Bajracharya, T. R., Shakya, S. R., Timilsina, A. B., Dhakal, J., Neupane, S., Gautam, A., & Sapkota, A. (2020). Effects of Geometrical Parameters in Gravitational Water Vortex Turbines with Conical Basin. Journal of Renewable Energy, 2020(Figure 1), 1–16. https://doi.org/10.1155/2020/5373784

Bernitsas, M. M., Raghavan, K., Ben-Simon, Y., & Garcia, E. M. (2006). VIVACE (Vortex induced vibration aquatic clean energy): A new concept in generation of clean and renewable energy from fluid flow. Volume 2: Ocean Engineering and Polar and Arctic Sciences and Technology, 2. https://doi.org/10.1115/omae2006-92645

Butera, I., & Balestra, R. (2015). Estimation of the hydropower potential of irrigation networks. Renewable And Sustainable Energy Reviews, 48, 140-151. https://doi.org/10.1016/j.rser.2015.03.046

Çengel, Y., & Cimbala, J. Fluid mechanics (3rd ed., p. 971). McGraw-Hill Education.

Graebel, W. (2007). Advanced fluid mechanics (1st ed., p. 368). Academic Press.

GUPTA, H. N. (2012). Fundamentals of internal combustion engines (2nd ed.). PHI Learning Pvt.

Dhakal, R., Bajracharya, T., Shakya, S., Kumal, B., Khanal, K., & Williamson, S. *et al.* (2017). Notice of Violation of IEEE Publication Principles: Computational and experimental investigation of runner for gravitational water vortex power plant. 2017 IEEE 6Th International Conference On Renewable Energy Research And Applications (ICRERA), 9. https://doi.org/10.1109/icrera.2017.8191087

Ersoy, S. (2014). Vortex with the Formation of Electricity Generation and System Modelling. International Journal Of Environmental Science And Development, 5(468), 152-154. https://doi.org/10.7763/ijesd.2014.v5.468

Huda, L. (2011). A study on the effect of dimensional oscillating part of vortex power plant using physical test [Master's thesis]. Department of Ocean Engineering Faculty of Marine Technology Institute Technology of Sepuluh.

Kaldellis, J. (2007). The contribution of small hydro power stations to the electricity generation in Greece: Technical and economic considerations. Energy Policy, 35(4), 2187-2196. https://doi.org/10.1016/j.enpol.2006.06.021

Khurmi, R. (1987). Textbook of Hydraulics, Fluid Mechanics and Hydraulic Machines (15th ed., p. 990). S Chand & Co.

Permana, D. W. (2011). Study effect of free surface on the oscillating part concerning to the performance lies vortex power: physical test phenomenological [Master's thesis]. Department of Ocean Engineering Faculty of Marine Technology Institute Technology of Sepuluh.

Rahman, M. M., Hong, T. J., & Tamiri, F. M. (2018). Effects of inlet flow rate and penstock's geometry on the performance of Gravitational Water Vortex Power Plant. Proceedings of the International Conference on Industrial Engineering and Operations Management, 2018-March, 2968–2976

Razan, J., Islam, R., Hasan, R., Hasan, S., & Islam, F. (2012). A Comprehensive Study of Micro-Hydropower Plant and Its

Potential in Bangladesh. ISRN Renewable Energy, 2012, 1-10. https://doi.org/10.5402/2012/635396

Saleem, A. S., Cheema, T. A., Ullah, R., Ahmad, S. M., Chattha, J. A., Akbar, B., & Park, C. W. (2020). Parametric study of single-stage gravitational water vortex turbine with cylindrical basin. Energy, 200, 117464. https://doi.org/10.1016/j.energy.2020.117464

Singh, P., & Nestmann, F. (2009). Experimental optimization of a free vortex propeller runner for micro hydro application. Experimental Thermal and Fluid Science, 33(6), 991-1002. https://doi.org/10.1016/j.expthermflusci.2009.04.007

Sritram, P., & Suntivarakorn, R. (2017). Comparative study of small hydropower turbine efficiency at low head water. Energy Procedia, 138,646-650. https://doi.org/10.1016/j.egypro.2017.10.181

Ullah, R., Cheema, T. A., Saleem, A. S., Ahmad, S. M., Chattha, J. A., & Park, C. W. (2020). Preliminary experimental study on multi-stage gravitational water vortex turbine in a conical basin. Renewable Energy, 145, 2516–2529. https://doi.org/10.1016/j.renene.2019.07.128

White, F. (2011). Fluid mechanics (7th ed., p. 863). McGraw-Hill Education (India) Private Limited.

Yamaguchi, H. (2008). Engineering fluid mechanics (1st ed.). Springer.

Zotlöterer, F. (2011). Hydroelectric power plant. Germany. Patent No WO 2011051421A2.

CALL FOR PAPERS

MIJST invites to submit Unpublished, Original, and Innovative research works from any branch of Engineering, applied sciences, and related areas.

Submitted manuscripts will undergo a double-blind peer-review process. For submission of Manuscript template and authors' instructions, please visit journal website at:
https://mijst.mist.ac.bd/mijst/index.php/mijst/

MIJST offers a faster peer-review process. There will be no charges for Registration, Online submission, Publication of manuscripts, and access to the published articles. Best selected papers will also be awarded by MIJST.

ABOUT MIJST

MIST International Journal of Science and Technology (MIJST), published biannually (June and December), is a peer-reviewed open-access journal of the Military Institute of Science and Technology (MIST). This journal is a continuation of the 'MIST Journal of Science and Technology', published by MIST, under ISSN 1999-2009 from 2009 to 2011, ISSN 2224-2007 from 2012 to 2019, & E-ISSN 2707-7365 since 2020.

MIJST publishes original research findings as regular papers, review papers (by invitation). The Journal provides a platform for Engineers, Researchers, Academicians, and Practitioners who are highly motivated in contributing to the Engineering, Science, and Technology and Applied Sciences disciplines. MIJST welcomes contributions that address solutions to the specific challenges of the developing world.

The Journal is now indexed in the "DOI Crossref", "ISSN Portal", "BaglaJOL", "Creative Common", "Microsoft Academic Search", "Publons", "Semantic Scholar", "ScienceGate" and "Open Journal System" databases and is accessible through the Google Scholar. The journal is also planned to be registered under the Asian Citation Indexing, Directory of Open Access Journals (DOAJ), SCOPUS, and Emerging Source Citation Indexing (ESCI) in course of time. The Journal aims to be one of the leading journals of the Country and the Region for its contributions in the advancement of Science and Technology. Unpublished innovative world-class research papers under the following subject areas are invited. Contributions from other areas of Engineering and Applied Sciences are also welcome.

SUBJECT AREAS:

- **AEROSPACE AND AVIONICS ENGINEERING**
- **APPLIED PHYSICS & SCIENCE**
- **ARCHITECTURE**
- **BIOMEDICAL ENGINEERING**
- **CHEMISTRY**
- **CIVIL ENGINEERING**
- **COMPUTER SCIENCE AND ENGINEERING**
- **ELECTRICAL, ELECTRONIC AND COMMUNICATION ENGINEERING**
- **ENVIRONMENTAL, WATER RESOURCES, AND COASTAL ENGINEERING**
- **INDUSTRIAL AND PRODUCTION ENGINEERING**
- **MATERIALS SCIENCE & ENGINEERING**
- **MECHANICAL ENGINEERING**
- **NAVAL ARCHITECTURE AND MARINE ENGINEERING**
- **NUCLEAR SCIENCE & ENGINEERING**
- **PETROLEUM AND MINING ENGINEERING**

E-ISSN: 2707-7365

Journal URL